BJ Biomolecules

Biochem. J. (2014) **464**, 23–34 (Printed in Great Britain) doi:10.1042/BJ20140409

Nucleotide binding triggers a conformational change of the CBS module of the magnesium transporter CNNM2 from a twisted towards a flat structure

María Ángeles Corral-Rodríguez*, Marchel Stuiver†, Guillermo Abascal-Palacios*, Tammo Diercks*, Iker Oyenarte*, June Ereño-Orbea*, Alain Ibáñez de Opakua*, Francisco J. Blanco*‡, José Antonio Encinar§, Vojtêch Spiwok‖, Hiroyuki Terashima¶, Alessio Accardi¶, Dominik Müller† and Luis Alfonso Martínez-Cruz*[1]

*Structural Biology Unit, Center for Cooperative Research in Bioscience (CIC bioGUNE), Technology Park of Bizkaia, 48160 Bizkaia, Spain
†Department of Pediatric Nephrology, Charité Universitäts Medizin, Berlin, 13353 Berlin, Germany
‡IKERBASQUE, Basque Foundation for Science, 48011 Bilbao, Spain
§Instituto de Biología Molecular y Celular, Universidad Miguel Hernández, Avda. del Ferrocarril s/n, 03202 Elche (Alicante), Spain
‖Department of Biochemistry and Microbiology, Institute of Chemical Technology, Prague, Technicka 3, Prague 6, 16628, Czech Republic
¶Department of Anesthesiology, Weill Cornell Medical College, Weill Cornell Medical College, 1300 York Avenue, NY, NY 10065, U.S.A.

Recent studies suggest CNNM2 (cyclin M2) to be part of the long-sought basolateral Mg^{2+} extruder at the renal distal convoluted tubule, or its regulator. In the present study, we explore structural features and ligand-binding capacities of the Bateman module of CNNM2 (residues 429–584), an intracellular domain structurally equivalent to the region involved in Mg^{2+} handling by the bacterial Mg^{2+} transporter MgtE, and AMP binding by the Mg^{2+} efflux protein CorC. Additionally, we studied the structural impact of the pathogenic mutation T568I located in this region. Our crystal structures reveal that nucleotides such as AMP, ADP or ATP bind at only one of the two cavities present in $CNNM2^{429–584}$. Mg^{2+} favours ATP binding by alleviating the otherwise negative charge repulsion existing between acidic residues and the polyphosphate group of ATP. In crystals $CNNM2^{429–584}$ forms parallel dimers, commonly referred to as CBS (cystathionine β-synthase) modules. Interestingly, nucleotide binding triggers a conformational change in the CBS module from a twisted towards a flat disc-like structure that mostly affects the structural elements connecting the Bateman module with the transmembrane region. We furthermore show that the T568I mutation, which causes dominant hypomagnesaemia, mimics the structural effect induced by nucleotide binding. The results of the present study suggest that the T568I mutation exerts its pathogenic effect in humans by constraining the conformational equilibrium of the CBS module of CNNM2, which becomes 'locked' in its flat form.

Key words: ancient conserved domain protein 2 (ACDP2), cyclin M2, cystathionine β-synthase (CBS) domain, hypomagnesaemia, magnesium homoeostasis.

INTRODUCTION

Magnesium (Mg^{2+}), the most abundant divalent cation in cells, is essential for life and has a crucial function in many biological processes such as ATP consumption, nucleic acid synthesis, enzyme function and neuronal transmission [1,2]. Mg^{2+} is unique among divalent cations in that it has the smallest ionic radius and the largest hydrated radius, thus requiring the action of specialized proteins known as Mg^{2+} transporters to be shuffled into and out of cells and intracellular organelles by mechanisms that differ from those used by other ions [3–11]. Dysfunction of Mg^{2+} handling is linked to different pathologies including osteoporosis, diabetes, hypertension, neurological disorders and immunodeficiency [12,13]. To avoid the severe consequences of Mg^{2+} deficiency, the body possesses a specialized system that keeps Mg^{2+} serum levels within narrow limits. The gross absorption of Mg^{2+} takes place in the intestinal epithelia, and is complemented by a reabsorption in the kidney. There, 60–70 % of the Mg^{2+} dissolved in the pre-urine is reabsorbed paracellularly in the TAL (thick ascending limb of the loop of Henle), whereas fine-tuning of serum Mg^{2+} levels occurs via active transcellular Mg^{2+} reabsorption at the DCT (distal convoluted tubule) of the nephron. In the DCT epithelium, Mg^{2+} is transported from the pre-urine side by the apical TRPM6 and TRPM7 (TRPM is transient receptor potential melastatin) channels, through the cytosol, and secreted via an as yet unidentified basolateral extrusion machinery to the blood side [14].

Interestingly, mutations in *CNNM2* (cyclin M2) cause familial dominant hypomagnesaemia [MIM613882] [15], a human disorder characterized by renal Mg^{2+} wasting that may lead to symptoms of Mg^{2+} depletion such as tetany, seizures and cardiac arrhythmias [16]. The data showed a predominant basolateral CNNM2 expression of cyclin M2 (CNNM2) in the DCT [16,17] suggesting that CNNM2 could be (part of) the Mg^{2+} extruder or, alternatively, regulate it. On the other hand, mutations in *CNNM4*, the closest homologue of *CNNM2*, have clinical consequences that are limited to retinal function and biomineralization, and are considered the cause of autosomal-recessive CRD (cone-rod dystrophy) with amelogenesis imperfecta [MIM217080] [18,19]. In support of a role for CNNM2 in the basolateral extrusion of Mg^{2+}, a study by Yamazaki et al. [20] demonstrated that its homologue CNNM4 is responsible for the extrusion of Mg^{2+} by intestinal epithelial cells. CNNM4 apparently meets this need by exchanging Mg^{2+} with Na^{+} without energy input.

CNNM2 and CNNM4 belong to the cyclin M family (CNNMs), also referred to as ACDPs (ancient conserved domain proteins),

Abbreviations: ACDP, ancient conserved domain protein; ADPNP, 5′-adenosyl-β,γ-imidodiphosphate; CBS, cystathionine β-synthase; cNMP, cyclic nucleotide monophosphate; CNNM, cyclin M; CSP, chemical shift perturbation; DCT, distal convoluted tubule; SPR, surface plasmon resonance; TRPM, transient receptor potential melastatin; WT, wild-type.

[1] To whom correspondence should be addressed (email amartinez@cicbiogune.es).

The corresponding atom co-ordinates have been deposited in the PDB with access codes 4IYS, 4P1G, 4IY0, 4P10 and 4IY4.

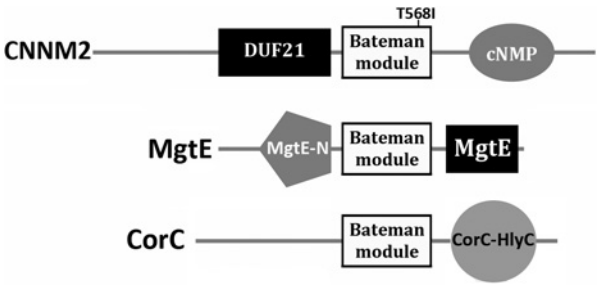

Figure 1 Domain distribution of CNNM2, MgtE and CorC

In CNNM2, the Bateman module (white), consisting of a pair of CBS motifs [45–48], connects with the transmembrane region (DUF21 domain, in black) through its N-terminal α-helix. CorC is structurally equivalent in this regard. The location of the hypomagnesaemia-causing mutation T568I [16,17] is indicated. In contrast, in MgtE the Bateman module connects with the transmembrane region through its C-terminal α-helix.

a poorly studied family of putative Mg^{2+} transporters in mammals [3,14,21]. In humans, CNNMs are encoded by four genes, *CNNM1–CNNM4* [3,22], and are evolutionarily expressed throughout development and in all adult tissues except for CNNM1, which is mainly expressed in the brain [16,22,23].

All CNNMs show very strong homology with the bacterial CorC and yeast Mam3p proteins that are involved in Mg^{2+} efflux, and Co^{2+} resistance and Mn^{2+} toxicity respectively [24,25].

Structurally, CNNMs are multidomain proteins that contain an extracellular N-terminal domain preceding a DUF21 transmembrane domain of unknown function (Pfam code PF01595) and a 'Bateman module' that includes a tandem of interleaved CBS (cystathionine β-synthase) motifs, CBS1/2 [22,26–28] (Figure 1). The structural difference between CorC and CNNM proteins lies in their C-terminal motifs. While CorC presents a HlyC domain involved in binding divalent cations (PDB codes 2R8D, 2P4P, 2PLI and 2PLS), CNNMs contain a cNMP (cyclic nucleotide monophosphate)-like binding domain (Pfam code PF00027) similar to that observed in some ion channels and cNMP-dependent kinases [29] (Figure 1). At present, the function of the Bateman module of CNNM2 remains unknown. However, taking into account that the equivalent region in CorC is involved in AMP binding and Mg^{2+} concentration sensing by the bacterial transporter MgtE [30–32], it is not unreasonable to assume that this Bateman module might similarly represent a region for interaction with metal ions and/or nucleotides in CNNMs.

Alternative to its function as a Mg^{2+} transporter [3,11,21–23,33], recent findings suggest that CNNM2 might act as a sensor for Mg^{2+} that indirectly regulates other Mg^{2+} transporters [16]. However, no direct evidence for CNNM2 interaction with metal ions (an obligate requirement for Mg^{2+} sensing and/or transport) and/or small molecules has been demonstrated to date, and the information is limited to biocomputational modelling [17].

With the aim to gain insight into the molecular mechanisms by which CNNM2 regulates Mg^{2+} homoeostasis, we have recently initiated a structural study to explore the ligand-binding capacity and conformational space of human CNNM2 and its closest homologue CNNM4 [34,35]. In the present paper we describe the crystal structure of the Bateman module of CNNM2 (residues 429–584), from which we derive a putative molecular mechanism by which nucleotide binding, involving Mg^{2+} ions, modulates the activity of this protein. We furthermore analyse the crystal structure of the T568I mutant that was shown to cause familial dominant hypomagnesaemia [16,17].

EXPERIMENTAL

Cloning, mutagenesis and purification

The $CNNM2^{429–584}$ and T568I_$CNNM2^{429–584}$ proteins were obtained following the protocol described in [35] with some modifications. The T568I_$CNNM2^{429–584}$ mutant was generated with the QuikChange® mutagenesis kit (Stratagene), using the pET101D plasmid as a template. The primers used to introduce the mutation were 5′-TGAAGTTCTGGGAATTGTCATCT-TGGAAGATGTGATTGAAG-3′ and 5′-CTTCAATCACATC-TTCCAAGATGACAATTCCCAGAACTTCA-3′. The plasmids obtained were transformed into *Escherichia coli* strain BL21-Codon Plus (Stratagene) for overexpression of ^{15}N-labelled $CNNM2^{429–584}$ for NMR analysis. The procedure was slightly modified with respect to that used for the WT (wild-type) protein according to the protocol of Marley et al. [36]. After growth at 37 °C in LB medium containing 0.1 mg/ml ampicillin to a D_{600} of 0.6, the culture was concentrated 3-fold in M9 medium with $^{15}NH_4Cl$ and 0.2 % glucose for ^{15}N-labelled His–$CNNM2^{429–584}$. The cultures were equilibrated at 20 °C for 30 min before overnight induction with 0.5 mM IPTG. Cells were lysed by sonication in 25 mM Hepes (pH 7.4), 0.4 M NaCl, 20 mM imidazole, 1 μM 2-mercaptoethanol, 0.1 mM PMSF, 1 mM benzamidine and 2.5 μg/ml DNase. After centrifugation at 35 000 ***g*** for 30 min, the extract was immediately subjected to affinity chromatography on a 1 ml HisTrap FF crude (GE Healthcare) column pre-equilibrated in the same buffer without DNase. Samples were eluted with 25 mM Hepes (pH 7.4), 0.4 M NaCl, 500 mM imidazole, 1 μM 2-mercaptoethanol, 0.1 mM PMSF and 1 mM benzamidine. The eluted single peak was then subjected to gel-filtration chromatography (HiLoad 16/60 Superdex-75; GE Healthcare) equilibrated in 150 mM Hepes (pH 7.4), 100 mM NaCl, 1 mM 2-mercaptoethanol, 0.2 % NaN_3, 1 mM benzamidine and 0.1 mM PMSF. Use of the metalloprotease inhibitor EDTA was avoided in order to preclude Mg^{2+} chelation in the titration experiments with Mg^{2+}. The resulting fractions with the target proteins were concentrated in an Amicon-15 centrifugal filter device (Millipore) to a final concentration of 30 mg/ml (∼1 mM).

Crystal structure determination

The native $CNNM2^{429–584}$ protein was purified and crystallized as described in [35]. Crystals of nucleotide-bound $CNNM2^{429–584}$ were obtained by co-crystallization with the corresponding nucleotides (AMP, ADP and ATP, with/without addition of 5 mM $MgCl_2$). Nucleotides were added to the crystallization drop at a final concentration of 10 mM, resulting in an approximate 1:10 molar ratio (protein/nucleotide). Crystals of the nucleotide–$CNNM2^{429–584}$ complexes were obtained by mixing equal volumes (0.5 μl) of the protein solution and a well solution containing 0.1 M sodium acetate (pH 4.6) and 3.0 M ammonium acetate. The final pH in the crystallization drop was 6.5. Crystals of the $CNNM2^{429–584}$ T568I mutant were obtained in 0.1 M sodium acetate (pH 4.6) and 2.5–2.8 M ammonium chloride. Refinement statistics and collected data are summarized in Table 1. Diffraction data were processed with HKL2000 [37]. Initial phases of $CNNM2^{429–584}$ were determined by molecular replacement methods with Phaser [38], using the MJ0100 protein (PDB code 3KPC [39]) as the search model. All models were refined with PHENIX [40] or REFMAC5 [41]. Non-crystallographic symmetry averaging between appropriate regions of the independent monomers in the asymmetric units was applied. Models were constructed with Coot [42]. The geometric

Table 1 Data collection and refinement processing statistics

One crystal was used per data set. Values in parentheses are for the highest resolution shell. $R_{sym} = \Sigma_{hkl} \Sigma_i |I_i(hkl) - <I(hkl)>| / \Sigma_{hkl} \Sigma_i I_i(hkl)$. $R_{work} = \Sigma |F_o - F_c| / \Sigma F_o$. $R_{free} = \Sigma |F_o - F_c| / \Sigma F_o$, calculated using a random 5 % of reflections that were not included throughout refinement. N/A, not applicable; a.u., asymmetric unit

Protein construct	CNNM2$^{429–584}$	CNNM2$^{429–584}$ + AMP	CNNM2$^{429–584}$ + ADP	CNNM2$^{429–584}$ + MgATP	CNNM2$^{429–584}$ (T568I)
Data collection and process					
Dimer conformer	Twisted	Flat	Flat	Flat	Flat
Beamline	ESRF ID23.1	Diamond i04	ESRF ID29	Homesource	ESRF ID14.1
Radiation wavelength (Å)	0.9793	0.9763	0.9793	1.5418	0.9334
Space group/PDB code	$P2_12_12$/4IYS	$I4_122$/4P1G	$I4_122$/4IY0	$P4_32_12$/4P1O	$P4_32_12$/4IY4
a (Å), b (Å), c (Å)	55.754, 64.453, 53.953	105.579, 105.579, 102.202	104.599, 104.599, 100.959	104.633, 104.633, 99.861	103.346, 103.346, 99.899
α (°), β (°), γ (°)	90, 90, 90	90, 90, 90	90, 90, 90	90, 90, 90	90, 90, 90
Molecules per a.u.	1	1	1	2	2
Resolution (Å)	54–1.8	28.2–2.6	42–1.9	33.1–3.1	46–2.9
R_{sym} (%)	4.5 (45.5)	3.7 (51.2)	4.9 (69.9)	8.0 (36.5)	9.6 (36.6)
Mean $I/\sigma I$	31.9 (2.9)	53.58 (5.6)	11.6 (2.2)	12.43 (3.55)	35.0 (6.2)
Completeness (%)	96.5 (96.4)	99.68 (97.0)	100 (95.9)	96.04 (94.5)	99.93 (100)
Redundancy	4.0 (3.8)	13.7 (13.6)	14.6 (14.9)	3.8 (3.6)	14.3 (14.7)
Mosaicity (°)	1.2	0.1	0.2	0.8	0.1
Refinement statistics					
Number of working reflections	18265	16872	22264	10514	12501
Number of test reflections	1719	1690	1138	1061	617
R_{work} (%)/R_{free} (%)	21.8/26.2	21.16/25.43	19.9/22.3	22.54/26.33	22.4/28.1
Number of atoms					
Protein	1261	1236	1224	2434	2427
Ligand	N/A	AMP (23)	27/4	ATP/Mg (62/2)	N/A
Water	135	0	116	0	0
Average B-factors (Å^2)					
Protein	37.8	91	47.6	68.8	60.9
Ligand	N/A	89.5	35.5/60.8	46.2/84.6	N/A
Water	41.0	N/A	50.32	N/A	N/A
RMSDs					
Bond lengths (Å)/angles (°)	0.011/1.297	0.007/1.153	0.016/1.71	0.004/0.756	0.002/0.537
Ramachandran plot statistics (%)					
Residues in most-favoured regions	98.7	100.0	98.7	99.0	97.3
Residues in additional allowed regions	1.3	0	1.3	1.0	2.7
Residues in disallowed regions	0	0	0	0	0

quality of the models was assessed with MolProbity [43], and illustrations were prepared with PyMOL (http://www.pymol.org). The corresponding atom co-ordinates have been deposited in the PDB with access codes 4IYS, 4P1G, 4IY0, 4P1O and 4IY4 (Table 1).

NMR analysis

For the NMR binding experiments we used samples of U-^{15}N isotopically labelled CNNM2$^{429–584}$ construct. To avoid bias in the titrations, we changed the conventional PBS (containing phosphate that might interact with Mg^{2+} or compete with ATP for binding) to 50 mM Hepes. Although 50 mM Hepes was sufficient for the $MgCl_2$ titrations, we increased its concentration to 150 mM for the titrations with the salts of ATP. To minimize autonomous ATP hydrolysis and to prevent a pH decrease from ATP hydrolysis, we used ADPNP (5′-adenosyl-β,γ-imidodiphosphate) (an enzymatically less-well-hydrolysable analogue of ATP; Sigma, catalogue number A2647) for the ATP titrations. The protein concentration was 200 μM in all experiments. The pH was set to 7.4, and verified at the end points of titration using a pH electrode. Moreover, the prominent ^{1}H-NMR signals of Hepes (at 3.77, 3.08, 2.91 and 2.85 p.p.m.) allowed for direct and sensitive *in situ* monitoring of the pH as their relative positions (notably, the signal at 2.91 p.p.m.) shift upon even slight pH changes. Thus the pH did not drop by more than 0.1 throughout the titrations. The samples furthermore contained 100 mM NaCl, 0.02 % NaN_3, 1 mM benzamidine and 0.1 mM PMSF to increase sample stability. All NMR experiments were carried out at 298 K on our 600 MHz Bruker AVANCE III spectrometer. For each titration point (0.1, 0.5, 1.0, 2.5 and 10 mM ATP or $MgCl_2$), we recorded (i) a 1D ^{1}H-NMR spectrum (with water suppression by excitation sculpting) to monitor the pH (on the Hepes signals) and the amount of ATP added, and (ii) a high-resolution 2D fast ^{15}N-HSQC (with water suppression by excitation sculpting and broad-band ^{1}H polarization flip-back) to monitor ligand-induced amide signal changes on the protein. Residues were considered as 'perturbed' by ligand binding, when their NMR signals experienced a CSP (chemical shift perturbation) larger than the average plus 1 S.D., or when their signal in the bound form could not be identified (due to intensity reduction beyond or to very large CSP).

RESULTS

Taking into account the known capacity of CBS domains to interact with nucleotides and/or metal ions [27,28,45–48] and former predictions suggesting the putative capacity of the Bateman module of CNNM2 to bind ATP (or MgATP) [17], we proceeded to analyse the independent and/or co-operative interaction of CNNM2$^{429–584}$ with these potential ligands. To that aim we first performed NMR titration experiments with observation of the protein's ^{15}N-HSQC fingerprint spectrum.

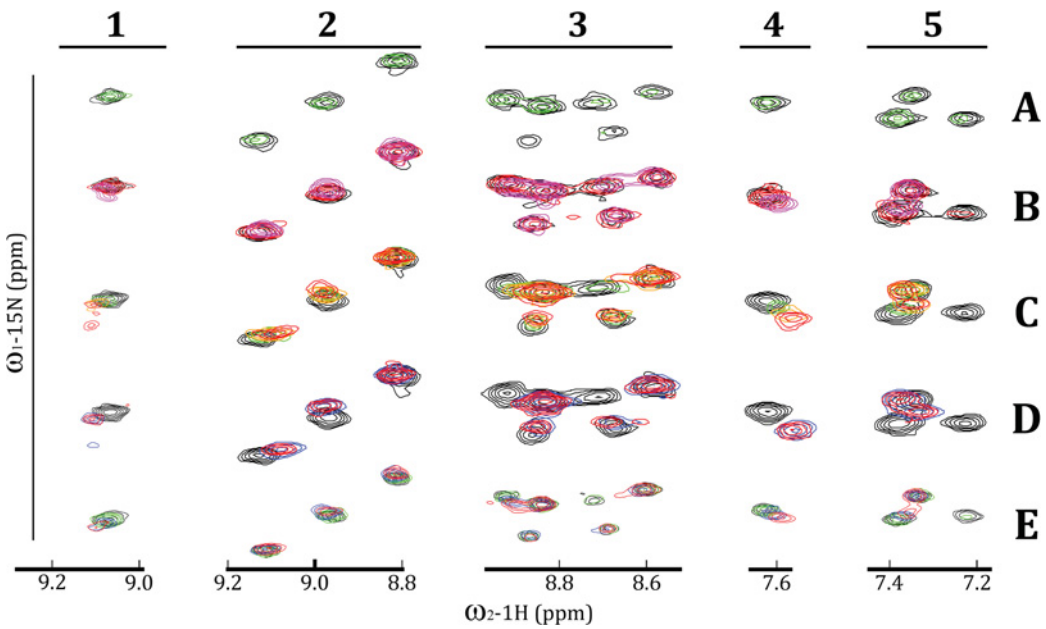

Figure 2 Effect of Mg^{2+} and/or nucleotides on the Bateman module of CNNM2

The Figure shows five representative groups of signals (columns 1–5) selected from the ^{15}N-HSQC CNNM2$^{429–584}$ protein spectrum and affected upon addition of Mg^{2+} and/or nucleotides to the protein solution. The signals obtained in the absence of Mg^{2+} (black) are overlapped with those obtained after addition of: (**A**) 2.5 mM $MgCl_2$ (green); (**B**) 0.5 mM ADPNP (red) and 10 mM ADPNP (magenta); (**C**) 2.5 mM ADPNP + 0.5 mM $MgCl_2$ (green), 2.5 mM ADPNP + 1 mM $MgCl_2$ (orange), and 2.5 mM ADPNP + 2.5 mM $MgCl_2$ (red); (**D**) 10 mM $MgCl_2$ + 2.5 mM ADPNP (red) or 2.5 mM ADPNP + 10 mM $MgCl_2$ (blue); and (**E**) 0.25 mM AMP (green), 2.5 mM AMP (blue) and 5 mM AMP (red). Note: no additional spectral changes are observed in the range 0.25–2.5 mM AMP. The protein concentration is 200 μM in all cases. The exact position of each group of signals (1–5) within the corresponding spectra is marked in Figures S1–S5.

Effect of Mg^{2+} on CNNM2$^{429–584}$

In the absence of ligands, [U-^{15}N]CNNM2$^{429–584}$ (50 μM in 150 mM Hepes, pH 7.4) shows a well dispersed ^{1}H-^{15}N spectrum with at least 126 backbone amide signals (out of 149 possible signals attributable to a unique conformation), indicative of a properly folded protein. Addition of increasing concentrations (0.5, 1, 2.0 and 2.5 mM) of $MgCl_2$ to CNNM2$^{429–584}$ produced barely no discernible spectral changes (three out of 120 well-resolved signals) (Supplementary Figure S1). The relative signal intensities decreased with increasing Mg^{2+} concentration, leading (at 2.5 mM $MgCl_2$) to attenuation and/or even complete disappearance of some signals (Figure 2 and Supplementary Figure S1). Signal attenuation is mostly accompanied by line broadening and/or splitting into numerous contiguous signals, attesting to slow exchange between Mg^{2+}-bound and free protein and/or increased conformational heterogeneity. In contrast, only a few signal intensities appear to increase. Gradual shifting of some signals (being the more typical and significant indicator of weak ligand binding) was barely observed (Supplementary Figure S1). Overall, our NMR titration studies reveal that the Bateman module of CNNM2 interacts only very weakly with Mg^{2+}, if added alone, with a $K_d > 10^{-2}$ M, and that the addition of Mg^{2+} causes a general conformational destabilization of CNNM2$^{429–584}$.

Effect of ATP on CNNM2$^{429–584}$

Next, we investigated the effect of adding ATP to the protein solution. To minimize autonomous ATP hydrolysis, we used ADPNP (an enzymatically less-well-hydrolysable analogue of ATP). ADPNP addition (0.1, 0.5, 1.0, 2.5 and 10 mM) produced more significant and numerous changes in the ^{15}N-HSQC spectrum of CNNM2$^{429–584}$, and at a distinctly lower concentration, than Mg^{2+}. Discernible spectral changes appeared between 0.5 and 2.5 mM ADPNP (eight out of 120 signals, 7 %, at 2.5 mM ADPNP; see those marked with black arrows in Supplementary Figure S2). Again, line broadening upon ADPNP addition is more prominent and abundant than signal shifting. The strong attenuation of several signals appears maximal at ~5 mM ADPNP, suggesting a K_d in the range 10^{-3}–10^{-2} M, which is in the range of the intracellular ATP concentration (1–10 mM) [49]. Still, a substantial number of signals also show distinct gradual signal shifting with increasing ADPNP concentration to 10 mM (30 out of 120 signals, 25 %, at 10 mM ADPNP; see also Figure 2 and Supplementary Figure S2), corroborating the estimated low K_d. Of special note, the vast majority of signals affected by ADPNP addition (Figure 2 and Supplementary Figure S2) are distinct from the few signals affected by Mg^{2+} addition (Figure 2 and Supplementary Figure S1), suggesting that different (but possibly vicinal) binding sites are occupied.

Mg^{2+}-dependent binding of ATP to CNNM2$^{429–584}$

Addition of increasing concentrations (0.5, 1, 2.0, 2.5 and 10 mM) of $MgCl_2$ to the mixture of CNNM2$^{429–584}$ + 2.5 mM ADPNP produced spectral changes in the protein's ^{15}N-HSQC fingerprint spectrum that occur at distinctly lower ATP concentration than in the absence of Mg^{2+} (Figure 2, and Supplementary Figures S2 and S3). As with Mg^{2+} or with ADPNP alone, signal line width and intensity are primarily affected (i.e. commonly signal narrowing with concomitant increase in intensity), but in this case changes in signal frequency are clearly more abundant, affecting 53 out of 120 well-resolved signals (i.e. 44 %) at 2.5 mM ADPNP + 2.5 mM $MgCl_2$ (Figure 2 and Supplementary Figure S3). Neither increasing the $MgCl_2$ concentration above 2.5 mM (i.e. to 10 mM), nor altering the order in which the ligands

were added to the protein solution (Supplementary Figure S4), involved further structural changes. Yet some spectral changes induced by Mg^{2+} and ADPNP co-addition make the ^{15}N-HSQC spectrum closely resemble the one obtained in the presence of high ADPNP concentrations (10 mM) alone (see signals 4C and 4D compared with 4B in Figure 2). Thus Mg^{2+} co-addition appears to reinforce and stabilize the spectral effects of ADPNP binding by CNNM2$^{429–584}$ (Figure 2, and Supplementary Figures S2–S4). This positive co-operative effect of Mg^{2+} upon ADPNP binding may derive from the cation's effect of increasing the protein's conformational heterogeneity (see above), where some of the newly populated conformations would be more favourable for ADPNP binding (i.e. Mg^{2+} binding would facilitate a conformational selection mechanism for ADPNP binding). Since ADPNP and Mg^{2+} binding affect largely different sets of CNNM2$^{429–584}$ signals, their binding sites do not (fully) overlap, and Mg^{2+} could therefore be considered an allosteric activator for ADPNP binding. It is, however, also possible that Mg^{2+} acts through conformational selection on ADPNP. This confirms previous reports in the literature of weak Mg^{2+} chelating by adenine, mainly involving the γ- and β-phosphate groups, and assisted by the basic N-7 of the purine [50]. Additionally, an elevated concentration of Mg^{2+} ions may neutralize otherwise repulsive forces between acidic clusters of the protein and the polyphosphate chain of ATP, thus contributing to stabilize the nucleotide within a concrete protein cavity. In this regard, we analysed whether a shorter polyphosphate chain in the nucleotide, with nominally less negative charge than ATP, favours (or not) the protein–ligand interaction. As shown in Figure 2 and Supplementary Figure S5, addition of increasing concentrations (0, 0.5, 1.0, 2.5 and 5 mM) of AMP to the protein solution indeed revealed changes in the ^{15}N-HSQC fingerprint spectrum (20 out of 123 well-resolved signals, 16 %) that resemble those obtained at higher (10 mM) ADPNP concentrations (see signals 1B compared with 1E, or 4B compared with 4E in Figure 2) or, alternatively, obtained by co-addition of ATP and Mg^{2+} (see, for instance, signals 2C and 2D compared with 2E, or 4C and 4D compared with 4E in Figure 2). We should note that the addition of Mg^{2+} to the AMP–protein solution did not involve further structural changes, and that spectral changes induced by AMP occur at lower concentrations than those triggered by ATP. These results support a positive effect of Mg^{2+} in reducing the charge repulsion between the protein and the nucleotide to favour ligand binding.

Despite the well-known preference of CBS domains to bind adenosine derivatives [46,47], the weak interaction observed between CNNM2$^{429–584}$ and ATP, prompted us to check whether CNNM2$^{429–584}$ has higher affinity for guanosine derivatives. However, no discernible changes were observed in the ^{15}N-HSQC spectrum upon addition of GTP (or GDP) even when these molecules were added in high excess (up to 10 mM), either in the absence or in the presence of Mg^{2+} (10 mM $MgCl_2$).

Crystal structure of CNNM2$^{429–584}$

With the aim to explore the structural basis for the detected interactions, we solved the crystal structure of WT-CNNM2$^{429–584}$ in the presence and in the absence of nucleotides and/or Mg^{2+}. The overall structure show the fold for a Bateman module made up of two consecutive CBS motifs (CBS1 and CBS2) preceded by flexible linkers (HA and HB) that comprise residues Lys^{444}–Cys^{456} and Asp^{506}–Leu^{522} respectively (Figures 3A and 3B). CBS1 and CBS2 comprise, approximately, residues Phe^{457}–Pro^{505} and His^{523}–Lys^{578} respectively. Both motifs with $\beta\alpha\beta\beta\alpha$ folds contact each other via their three-stranded β-sheets (where the first two β strands run parallel, the third one antiparallel), and both long edges of this bilayer interface are suggested nucleotide-binding sites (Figure 3) [46,47]. Furthermore, each N-terminal helix of the flexible linker (HA or HB) forms an integral part of the other CBS motif by antiparallel packing between its C-terminal β-strand (β3 or β6) and α-helix (H4), such that both CBS motifs form a nested overall structure with pseudo-C_2 symmetry. Despite low internal sequence homology, both CBS motifs structurally differ only in that the same secondary structure elements are less well defined and extended in CBS1. Thus the β-sheet in CBS1 is smaller, the N-terminal helix HA is shorter and adopts a stretched 3_{10} conformation, and H2, also a 3_{10} helix, is split into two sections by an extended bend. Our CNNM2$^{429–584}$ construct also comprises the native N-terminal extension (Leu^{432}–Thr^{443}) that connects to the preceding DUF21 transmembrane domain and forms an α-helix (H0) which packs against helices H3 and H4 of CBS2 and is orientated towards the transmembrane region (Figure 3). As described below, the orientation of this helix can vary which, together with a concomitant shift of helix H4, represents the major structural change observed in the protein monomer. An extensive network of direct or water-mediated hydrogen-bond interactions involving residues Thr^{479}, Arg^{480}, His^{520}, His^{544}, Thr^{568}, Glu^{570} and Asp^{571}, together with a salt bridge between Arg^{480} (N-terminus of strand β2) and Glu^{570} (first turn in helix H4) strengthens the interaction between both CBS motifs, and plays a crucial role in maintaining their relative orientation in the Bateman module.

Nucleotide binding occurs at site S2 of the Bateman module

The structure of CNNM2$^{429–584}$ features two major cavities (S1 and S2) at opposite ends of the central β-sheets (Figure 3), which are equivalent to the canonical clefts that usually accommodate nucleotides in other CBS domain proteins [39,45–48]. These cavities are formed by three structural blocks: (i) residues from the linker regions preceding the first β-strand (β1/β4) of each CBS domain, (ii) residues from the second β-strand (β2/β5), and (iii) residues located at the third strands (β6/β3) of each β-sheet and the first two turns of the following helices (H4/H2$_A$) (Figure 3). On the basis of our current structural knowledge of CBS domains, both clefts in CNNM2$^{429–584}$ may potentially host a nucleotide. Site S1 shows a hydrophobic cage (residues Ile^{491}, Leu^{494}, Phe^{496}, His^{520}, Leu^{522}, His^{544}, Leu^{545}, Ala^{546} and Ile^{547}) to accommodate the adenine ring, a conserved aspartate residue (Asp^{499}) for interaction with ribose, and several positively charged residues (Arg^{480}, Lys^{498} and His^{544}) plus a threonine residue (Thr^{479}) for stabilizing a phosphate moiety (Supplementary Figure S6). On the opposite side of the Bateman module, S2 likewise features a hydrophobic environment (Phe^{457}, Met^{458}, Tyr^{478}, Ile^{481}, Leu^{545}, Ile^{566} and Val^{567}), a conserved aspartate residue (Asp^{571}) and a threonine residue (Thr^{568}), but an acidic cluster (Glu^{570}, Asp^{571} and Glu^{574}) on α-helix H4 (Figure 4). In principle, charge repulsion between this acidic cluster and the nucleotide's phosphate moieties should disfavour nucleotide binding. The negative charge may, however, be neutralized or even inverted by (i) local cation binding, (ii) the positive dipole end of helix H4, and (iii) the nearby Arg^{480} that forms a salt bridge with Glu^{570} (Figure 4). Indeed, co-crystallization of CNNM2$^{429–584}$ with metal ions and/or nucleotides (AMP, ADP and ATP) never yielded ligand binding at site S1 (Supplementary Figure S6); instead, all obtained holo structures contained nucleotide bound only at site S2 (Figure 4). Preference for S2 may be due to better accessibility granted by the HA1-β1 connecting loop, as opposed to the analogous HB-β4 connecting loop that partially occludes the S1 cavity (Figure 3 and Supplementary Figure S6). Moreover, steric hindrance by residues Phe^{496} and Lys^{498} (which

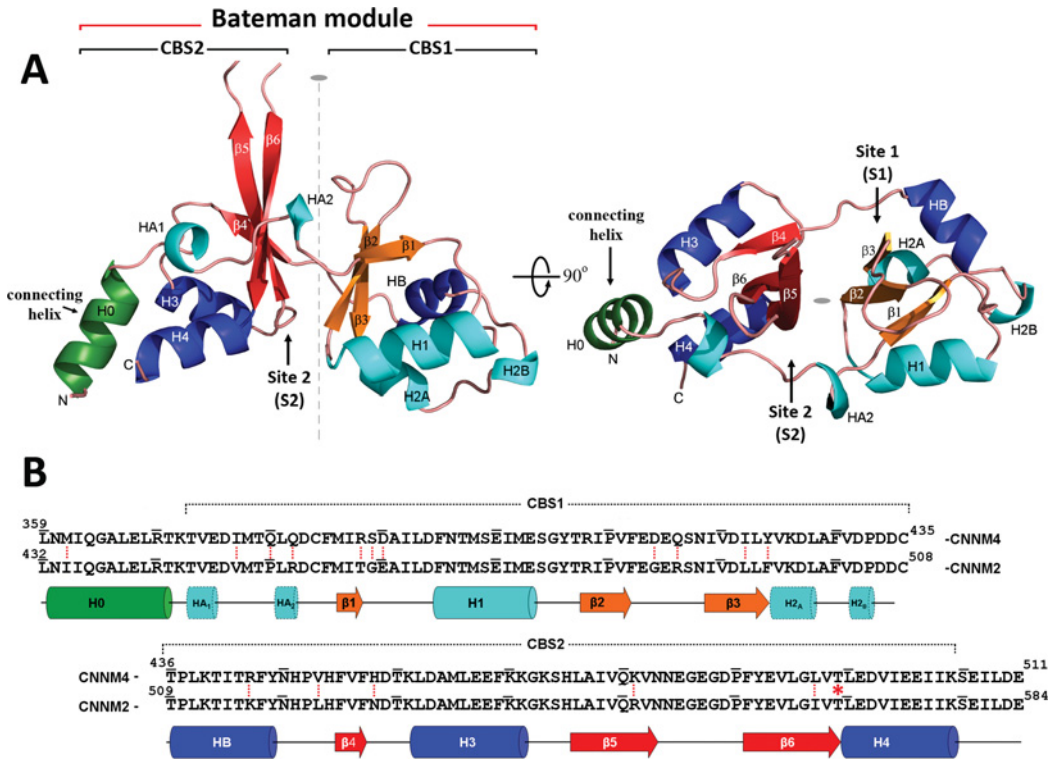

Figure 3 Crystal structure of the CNNM2$^{429–584}$ monomer

(**A**) CNNM2$^{429–584}$ adopts the overall fold of a Bateman module and contains two consecutive CBS motifs (CBS1, residues 445–508; CBS2, residues 509–578). A long loop, which is disordered in most of the crystals analysed, connects strands β5 and β6. Of note, the equivalent loop in the magnesium transporter CNNM3 mediates the interaction with protein tyrosine phosphatase PRL-2 [58]. The H0 helix connects the flexible linker preceding the Bateman module with the DUF21 transmembrane region in the full-length protein. Of the two main cavities present in the protein (referred to as S1 and S2), only S2 hosts nucleotides (see Figure 4). The pseudo two-fold symmetry axis relating CBS1 and CBS2 is indicated by a broken line. (**B**) Sequence alignment of the Bateman modules region in CNNM2 and its closest homologue CNNM4. The secondary structure elements shown on top of the sequences are extracted from the crystal structures. Vertical red broken lines indicate the few residues that are different between the CNNM2 and CNNM4 proteins in this region. Location of Thr^{568} affected by the pathogenic mutation T568I is marked with an asterisk.

occupy positions equivalent to Thr^{568} and Glu^{570} in S2) may contribute to impaired nucleotide binding at S1 (Supplementary Figure S6). The apo structure shows that Thr^{568} at site S2, at the C-terminus of strand β6 in the CBS2 motif, is at the centre of an extensive network of direct or water-mediated hydrogen-bond interactions involving Thr^{451}, Thr^{479}, Glu^{570} and Asp^{571}, and helps to orientate Glu^{570} in forming a salt link with Arg^{480}, located at the opposite side of the crevice (Figure 4). Nucleotide binding of AMP, ADP or ATP at S2 disrupts the Glu^{570}–Arg^{480} salt bridge and the network of interactions centred on Thr^{568}, and induces a relative shift of both CBS motifs that results in an expansion of the Bateman module. The nucleotide's adenine ring remains stacked between Tyr^{478} and Ile^{566} in a hydrophobic pocket comprising Pro^{482}, Ile^{481}, Cys^{456}, Phe^{457} and Met^{458} (Figure 4), whereas the ribose ring forms hydrogen bonds with the side chains of Thr^{568} and Asp^{571}. In contrast, the orientation of the nucleotides' ribose ring and the polyphosphate chain varies depending on the number of phosphates attached to its adenosyl group and, hence, total negative charge. In a complementary manner, there are subtle differences mainly in the side-chain orientation of polar amino acids at site S2 (Figure 4). Although the guanidinium group of Arg^{480} always forms a stabilizing salt bridge with the common α-phosphate, the Thr^{479} hydroxy group detaches from Arg^{480} to instead engage in hydrogen-bonding with the β-phosphate of ADP or ATP and with the γ-phosphate present only in ATP; the released Glu^{570} carboxy group rotates slightly upon AMP binding, but is significantly repelled upon ADP or ATP binding; and the more distant Glu^{574} side chain flips away only from bound ADP. Thus all residues from the acidic cluster (Glu^{570}, Asp^{571} and Glu^{574}) respond strongly to nucleotide binding at site S2, presumably for both steric and electrostatic (repulsive) reasons, in a manner that discriminates between distinct phosphorylation states.

CNNM2$^{429–584}$ forms dimers that suffer a conformational change upon nucleotide binding

In our crystal structures, two Bateman modules of CNNM2$^{429–584}$ associate as a head-to-head dimer (a 'parallel CBS module') (a detailed explanation on how Bateman modules usually associate is given in [47]) where both CBS1 and CBS2 motifs pack against their equivalent in the other monomer. Within the crystal, and in the absence of bound nucleotide, the CNNM2$^{429–584}$ dimer adopts a Y-shaped ('twisted') conformation (Figure 5A and Table 1), where both CBS2 domains still contact each other closely while the CBS1 motifs have separated and retain only scarce hydrophobic contacts between residues at the C-terminus of helix HB (Phe^{517} and Tyr^{518}) and a hydrogen bond between Lys^{498} (helix H2$_A$) and Gly^{541} (H3). Upon binding of nucleotides (AMP, ADP, ATP or MgATP) at site S2, however, the CNNM2$^{429–584}$ dimer adopts a disc-like ('flat') structure in which also both CBS1 motifs interact symmetrically through hydrophobic and hydrogen-bond contacts between helices H1 and H2$_A$/H2$_B$ (Figure 5B), thereby mimicking the holo structures of CorC (the bacterial orthologue of CNNM proteins; PDB codes 4HG0 and 3JTF) with AMP, and MgtE with Mg^{2+} [30–32].

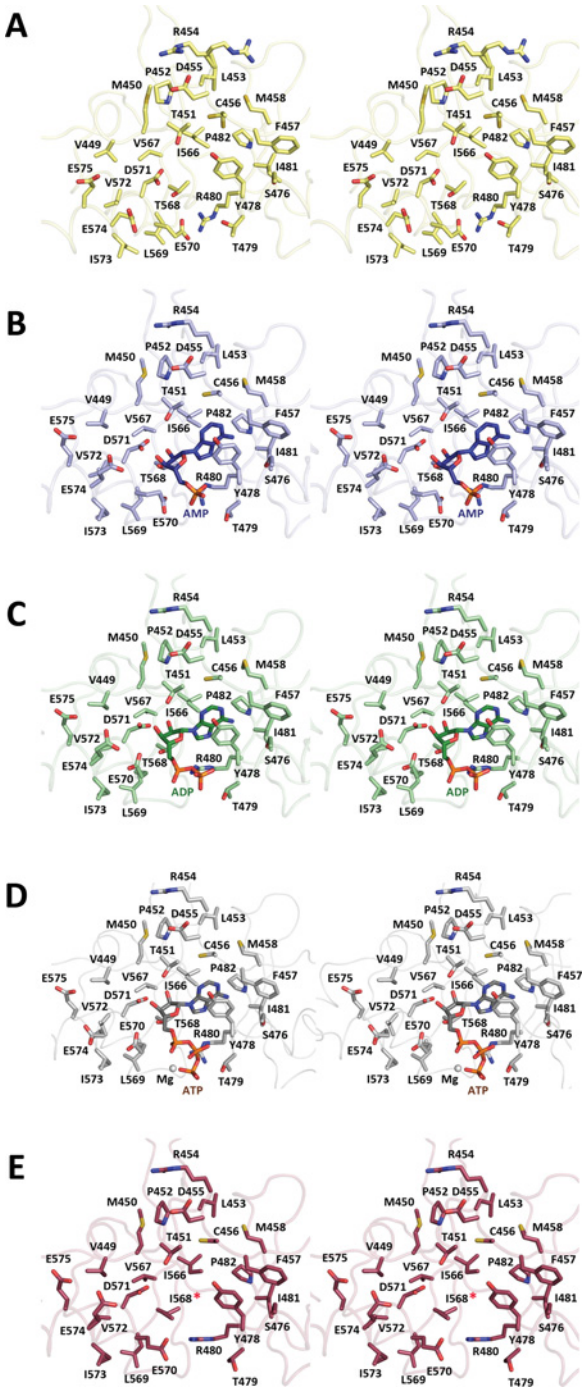

Figure 4 Stereo pairs of the S2 nucleotide-binding site of CNNM2$^{429–584}$ in the apoprotein (yellow), and in the AMP (blue), ADP (green) and Mg-ATP (silver, where the Mg^{2+} ion bound to ATP is represented with a grey sphere) complexes

The lowest stereo pair corresponds to the S2 site of mutant T568I.

In the 'flat' form, the bipartite dimer interface (comprising both CBS1–CBS1* and CBS2–CBS2* interfaces) is stabilized by an extensive network of hydrophobic side-chain interactions. Interactions between CBS1 and CBS1* motifs are symmetrical, with reciprocal H1–H2* and H2–H1* helix contacts involving residues Phe^{467}, Met^{470}, Met^{474}, Val^{497}, Lys^{498}, Leu^{500}, Phe^{502}, Val^{503} and Pro^{505}. Similarly, interaction between both well-structured CBS2 motifs is largely symmetrical, with reciprocal H3–H4* and H4–H3* helix contacts involving Leu^{535} (H3) and Leu^{569}, Ile^{573}, Ile^{576} and Ile^{577} (H4).

Among the distinct dimer forms, monomers differ markedly in the orientation of helix H0 from the N-terminal extension that does not form part of the canonical Bateman module, and of helix H4 at the C-terminal end of the CBS2 motif (Figure 5). In our apo-CNNM2$^{429–584}$ structure, H0 participates in the CBS2 dimer interface via residues Ile^{434} and Ile^{435}. Upon dimerization, the H0 helices lie crossed in the 'twisted' dimer (Figure 5A), but run antiparallel in the 'flat' dimer (Figure 5B) where they show tight hydrophobic contacts for residues Ala^{431}, Leu^{432}, Ile^{434}, Ile^{435}, Ala^{438}, Leu^{439} and Leu^{441}. The crystal structures of CNNM2$^{429–584}$ furthermore indicate several salt bridges that possibly contribute to the high thermal stability observed by CD (results not shown). These include Glu^{430}–Lys^{539} (H0–H3), Glu^{440}–Lys^{444}, Glu^{462}–Lys^{512}–Glu^{485}, Asp^{499}–His^{520}, Glu^{536}–Lys^{540}–Glu^{537}, Glu^{554}–Arg^{550}–Glu^{562}, Glu^{575}–Lys^{444}–Glu^{580}, Lys^{578}–Glu^{575} and the notable Glu^{570}–Arg^{480} that disrupts upon nucleotide binding. The salt bridge Glu^{574}–Lys^{539} connects complementary monomers in apo-CNNM2$^{429–584}$, whereas Glu^{430}–Lys^{539} stabilizes the flat nucleotide-bound conformers. Apart from these directed salt bridges, clusters of complementary charged residues are found in the dipolar helix H3 (Glu^{536}, Glu^{537}, Lys^{540} and Lys^{542}), adjacent acidic helix H4 (Glu^{574} and Glu^{575}), and basic helix H0 (Lys^{444}) within CBS2.

The pathological mutation T568I impedes the interaction with nucleotides, but mimics the conformational effect of nucleotide binding

Overall, the crystal structures of apo and nucleotide-bound CNNM2$^{429–584}$ monomers show major differences that include helices H0 and H4 (in CBS2), the flexible linker region comprising helix HA_1, and the loop connecting helix H3 with strand $\beta5$ (in CBS1) (Figures 3 and 5). AMP, ADP and ATP induce similar structural effects (Figure 6). In the apo form, helices H0 and H4 run antiparallel, where H4 is closer to the S2 cavity, crosses with H4* of the second monomer (Figure 5) and is fixed by a network of polar interactions around Thr^{568}, Glu^{570} and Asp^{571}. Thr^{568} hydrogen bonds with Glu^{570} that in turn forms a salt bridge with Arg^{480}, and with Asp^{571} that contacts with Val^{449}, Met^{450}, Thr^{451} and Glu^{474} (Figure 4A). Hydrophobic interactions between Leu^{441}, Leu^{531}, Val^{572} and Ile^{581}, and a double salt bridge between Glu^{440}, Lys^{444} and Glu^{575} further stabilize the H4 orientation, particularly with respect to helix H0. Our crystal structures of holo-CNNM2$^{429–584}$ reveal that nucleotide binding in the S2 cavity causes electrostatic repulsion that affects most of the interactions described above. Thus it disrupts the salt bridge Glu^{570}–Arg^{480} by negative charge repulsion between the α-phosphate and the carboxy group of Glu^{570}, but also by salt bridging Arg^{480} with the α- and β-phosphates of the nucleotide (Figures 4B–4D). The polyphosphate chain orientation is further stabilized through hydrogen bonds with Thr^{568} and Thr^{479}. The negative charge repulsion caused by nucleotide binding is alleviated by shifting helix H4 to allow reorientating of Glu^{575} and Glu^{580} towards Lys^{444} and Lys^{578}. As a consequence, helix H0 moves from an antiparallel orientation with helix H4 to one with helix H0* from the complementary monomer, leaving an angle of approximately 45° between H0 and H4 (Figures 5 and 6). All of these structural rearrangements eventually transmit to the dimer interface, and result in a conformational change for the CBS module from a 'twisted' to a 'flat' conformation (Figures 5 and 6, and Supplementary Movies S1–S4).

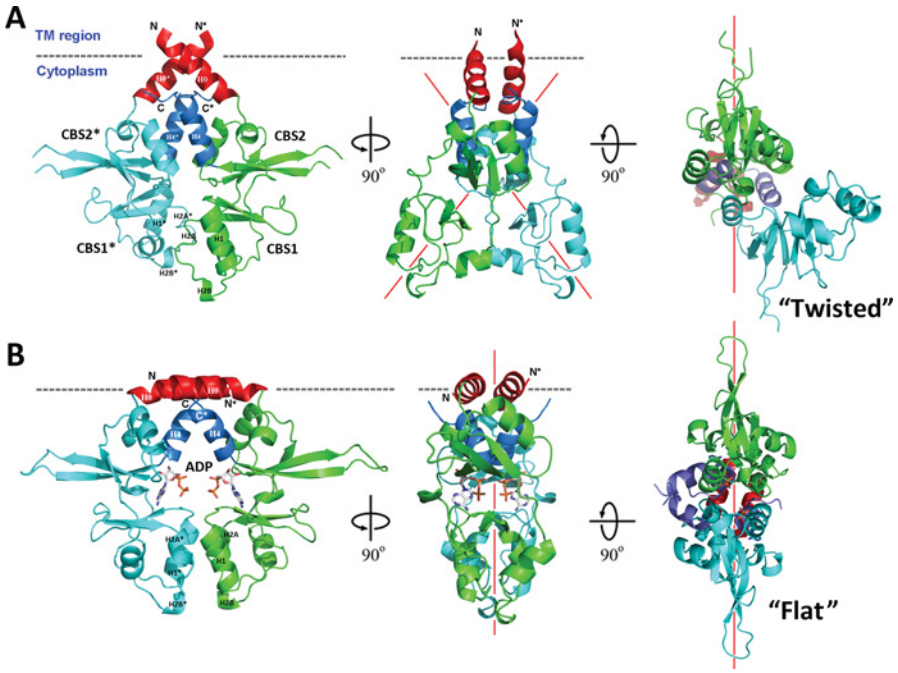

Figure 5 Conformations of the apo and nucleotide-bound CNNM2$^{429–584}$ complexes

The Figure shows three different views of the two different types of CNNM2$^{429–584}$ dimers that are present in our crystals: (**A**), a 'twisted' dimer in which one of the Bateman modules rotates away from the original plane containing the protein disc (see also Figure 6) and (**B**), a 'flat' disc-like dimer formed upon binding of AMP/ADP or Mg-ATP (the ADP is represented). These conformers represent the initial and final steps of the conformational change suffered by the CNNM2$^{429–584}$ dimer upon nucleotide binding. α-Helices H0 (red) and H4 (marine blue) are the main structural elements affected upon nucleotide binding in each monomer. The two complementary monomers are represented in cyan and green respectively.

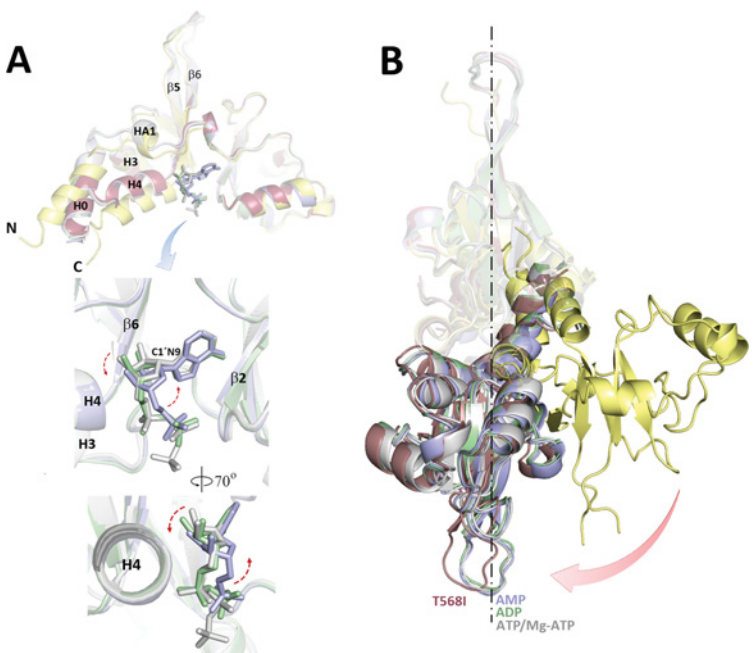

Figure 6 Effect of ligands and mutations on CNNM2$^{429–584}$

(**A**) Top panel: overlap of apo-CNNM2$^{429–584}$ (yellow), AMP-, ADP- and MgATP-bound CNNM2 (blue, green and silver respectively), and T568I mutant (red). The main distinct feature is the orientation of α-helices H0 and H4, and also of the short helical region HA_1. Bottom panel: magnified view of a section of two different views showing the rotation of the ribose ring of the bound nucleotides around the C1′–N9 bond. (**B**) Side view of the CNNM2$^{429–584}$ dimer showing the conformational change suffered upon binding of nucleotides to both monomers. The broken line represents a plane perpendicular to the image that contains the disc-like CNNM2$^{429–584}$ flat dimer. Of note, mutation T568I mimics the effect of nucleotide binding to site S2.

Remarkably, mutation of Thr^{568} to isoleucine, as found in patients suffering from familial dominant hypomagnesaemia [16] mimics the structural effect of nucleotide binding and stabilizes the 'flat' conformer (Figure 6). This can be explained by the central role of Thr^{568} in the network of polar interactions that stabilize the orientation of helices H4 and H0, as detailed above, and are lost by mutation to a hydrophobic isoleucine residue (Figure 4B). This more bulky residue also causes steric hindrance that pushes Glu^{570} from its original position (in apo WT-CNNM2$^{429–584}$), as by the cascade of electrostatic repulsions described above. Our crystal structures demonstrate that helices H0 and H4 reorientate in a co-ordinated manner, and are directly involved in the change from a 'twisted' to a 'flat' conformation of the CBS module (Supplementary Movies S1–S4). Thus the pathogenic T568I mutation locks the CNNM2$^{429–584}$ dimer in its 'flat' conformation (Figure 6), and probably impedes its return to the 'twisted' state.

Potential Mg^{2+}-binding sites

Our crystal structures revealed that CNNM2$^{429–584}$ contains several clusters of acidic residues (called M1 to M4 below) that might represent potential Mg^{2+}-binding sites. Cluster M1 (Thr^{568}, Glu^{570}, Asp^{571} and Glu^{574} in strand β6 and helix H4) is located at the canonical S2 cavity (Figure 4) and shows a similar geometry to that found in MgtE to bind cations Mg4, Mg5 and Mg7 [30,31]. As mentioned above, these residues are also involved in nucleotide binding. Interestingly, residue Thr^{568} occupies the same position as Thr^{244} in MgtE that participates in Mg^{2+}-binding [30,31] and, if mutated to isoleucine (T568I-CNNM2) is linked to the development of familial hypomagnesaemia [16,17]. Cluster M2 in CBS2 comprises residues within and near helix HA_1 (Thr^{445}, Glu^{447}, Asp^{448} and Asp^{528}), whereas clusters M3 and M4 in CBS1 include residues in the adjacent loops β1–H1 and β2–β3 (Glu^{462}, Glu^{485} and Glu^{487}) and around helix $H2_B$ (Asp^{504}, Asp^{506} and Asp^{507}) respectively.

Taking into account the effect of Mg^{2+} on CNNM2$^{429–584}$ (see NMR section), we explored whether Mg^{2+} binds at any of the acidic clusters revealed by the crystal structure. To that aim, we soaked CNNM2$^{429–584}$ protein crystals in solutions containing $MgCl_2$ (1–10 mM $MgCl_2$) or, alternatively, co-crystallized the protein in solutions containing the Mg^{2+} cation (1–10 mM $MgCl_2$). However, and despite the similarities observed between MgtE and CNNM2 in this protein region, all crystals of CNNM2$^{429–584}$ grown in the presence of $MgCl_2$ alone did not show residual electron density in the $F_o - F_c$ electron density maps that could be unequivocally attributed to Mg^{2+}. These data confirm the results obtained using NMR techniques mentioned above (Supplementary Figure S1). In contrast, co-crystallization of 1 mM CNNM2$^{429–584}$ with 5 mM $MgCl_2$ and 10 mM ATP yielded ternary CNNM2$^{429–584}$–MgATP complexes with MgATP bound at site S2 (Figure 4 and Supplementary Figure S7). The crystal structure reveals a Mg^{2+} cation interacting with the α- and γ-phosphate groups of ATP (Supplementary Figure S7), thereby stabilizing a bent conformation of the triphosphate group. In the absence of $MgCl_2$, no residual density that could be attributed to Mg^{2+} cations was detectable in the crystals.

DISCUSSION

In continuation of recent studies on how CBS domains regulate protein activity and how mutations in their sequence lead to human pathologies [16,17,28,34,35,45,46], we have explored the structure and ligand-binding capacity of the truncated CNNM2$^{429–584}$ protein comprising the Bateman module of CNNM2. This intracellular region [17] is structurally equivalent to the one present in the bacterial CorC and the MgtE proteins (Figure 1), where it binds AMP (PDB codes 4HG0 and 3JTF) and acts as Mg^{2+} sensor (PDB code 2YVY) respectively [30–32]. In MgtE, the Bateman module forms a head-to-head (parallel) dimer called a CBS module (see [30–32,47]) that switches from an 'open' to a 'closed' conformation upon Mg^{2+} binding without requiring additionally bound nucleotides [30–32]. This conformational change in the CBS module is transmitted to the transmembrane region of the transporter through the C-terminal α-helices connecting both Bateman modules with the transmembrane domains, thus regulating the Mg^{2+} intake. On the other hand, the AMP-bound complexes of CorC from *E. coli* (PDB code 4HG0) and the Bateman module of CorC from *Bordetella parapertussis* (PDB code 3JTF) show that CorC dimerizes into flat parallel CBS modules that host AMP at their S2 cavity. However, no apo form of CorC is available, limiting our knowledge about the structural impact of AMP binding.

Our crystal structures reveal similarities between CNNM2$^{429–584}$ and the Bateman modules of both CorC and MgtE. For instance, all form parallel dimers and are enriched in acidic residues. More interestingly, the canonical binding site S2 (Figure 4) between both constituent CBS domains is versatile enough to bind both metal ions (as in MgtE) and nucleotides (as in CorC). Beyond these common characteristics, however, we found that CNNM2$^{429–584}$ has topological and physicochemical features suggesting that it behaves more like prokaryotic CorC, while obeying a different regulatory mechanism from that of MgtE. This is supported by distinct orientations of the secondary structure elements connecting the transmembrane and intracellular regions (Figure 1) and, more importantly, a different distribution of acidic residue clusters (M1–M4) that might act as Mg^{2+}-binding sites, with the exception of M1 within the S2 cavity. In contrast with MgtE, most acidic clusters in CNNM2$^{429–584}$ participate in salt bridges to neutralize charge repulsion between monomers even without inclusion of Mg^{2+} ions. An exception is cluster M3 (with residues Asp^{504}–Asp^{506}–Asp^{507}) that concentrates negative charges at the connecting loop between helices $H2_B$ (in CBS1) and HB (in CBS2) (Figure 3). Despite no Mg^{2+} ions having been found at this cluster in our crystals, cluster M3 should not yet be discarded as a potential binding site for free Mg^{2+} ions since cations bound at this position would significantly neutralize the otherwise existing electrostatic repulsion between M3 clusters from complementary subunits in the flat protein conformer. Further studies are in progress to confirm this hypothesis.

Interestingly, ATP binding is clearly favoured in the presence of Mg^{2+} (Figure 2, and Supplementary Figures S3 and S4). Indeed, our X-ray complex structure reveals one Mg^{2+} cation ligated to the triphosphate moiety of CNNM2$^{429–584}$-bound ATP (Supplementary Figure S7). This chelation of Mg^{2+} by ATP is known to perform already in solution, i.e. Mg^{2+} directly interacts with nucleotides NP_i at physiological pH, and the prevailing interacting species is therefore the complex $[Mg{\cdot}NP_i]^{2-}$ (Z) [50]. There, Mg^{2+} directly binds to the γ- and β-phosphate groups, and additionally to the basic imidazole N-7 in purine nucleobases (although less tightly and primarily via a bridging water molecule). This macrochelate formation stabilizes an ATP conformation (i.e. a rotamer that buries the imidazole and exposes the pyrimidine ring) which might be favoured for binding by CNNM2$^{429–584}$. Additionally, the barrier to ligand entry is significantly reduced by Mg^{2+} co-binding, suggesting that negative charge repulsion between the acidic cluster M1 (Glu^{570}, Glu^{571} and Glu^{574}) (Figure 4 and Supplementary Figure S8) and the nucleotide's

polyphosphate chain might play a major role in inhibiting ligand entry.

The crystal structure of the AMP–, ADP– and MgATP–CNNM2$^{429–584}$ complexes provide the strongest evidence for specific nucleotide and Mg^{2+} binding to the Bateman module of CNNM2. Until now, both ATP (or MgATP) binding as well as its location, had been hypothesized based on computational models [17]. The high sequence identity between CNNM2 and CNNM4 strongly suggests that S2 also hosts MgATP in CNNM4. Our data show that nucleotide binding does not induce large structural changes in the CNNM2$^{429–584}$ monomer, except for local structural rearrangements of helices H0 and H4 near the dimeric interface (Figure 6). However, the structures reveal that these apparently small changes confer a remarkable conformational variability to the protein dimer, that varies from a 'twisted' to a 'flat' conformation under different circumstances (Figures 5 and 6, and Supplementary Movies S1–S4). Thus, in the absence of bound nucleotides, it preferably rests in a Y-shaped ('twisted') conformation (Figures 5 and 6). Conversely, binding of AMP, ADP or MgATP fosters the conformational equilibrium towards a disc-like 'flat' state (Figures 5 and 6, and Supplementary Movies S1–S4). The seemingly inconspicuous changes observed in the NMR titration experiments apparently contrast with the rather substantial change in the domain orientation in the crystal structure, but can be explained by the fact that only a small hinge region of the CBS module varies along the conformational change (Figure 5, and Supplementary Movies S1–S4).

Taking into account the central location of the Bateman module in the polypeptide chain (Figure 1), it seems reasonable to assume that the structural changes suffered by helix H0 are transmitted to the intermembrane region. Similarly, shifts in helix H4 probably affect the subsequent intracellular cNMP-binding domain.

Interestingly, the positioning of ATP and its surrounding amino acid residues within the S2 cavity, are somewhat reminiscent of the ATP-binding site of ABC transporters (Supplementary Figure S8) [51]. There a glutamate residue C-terminal to the Walker B motif and a conserved histidine residue of the Walker A motif, act as a linchpin holding together a complicated network of interactions that provide the framework that allows ATP hydrolysis [51]. The crystal structure of the ADP–CNNM2$^{429–584}$ complex indeed shows the Thr^{479}-OH group within Van der Waals distance to the nucleotide's β-phosphate, suggesting a direct Thr^{479}-O-β-phosphate bond (Figure 4 and Supplementary Figure S8). Moreover, and similar to endonuclease G [52], the conserved His^{544} and Arg^{480} (Supplementary Figure S8) are positioned so close to the polyphosphate chain that they might assist in ATP hydrolysis by activating a nucleophilic water molecule and neutralizing the phosphate leaving group. These structural similarities open the door for future experiments aimed at exploring the potential ATPase capacity of the Bateman module of CNNMs and its role in Mg^{2+} efflux. We speculate that reducing the electrostatic repulsion within the S2 site through ATP hydrolysis might be a possible mechanism by which Mg^{2+} is released from ATP (and thus from the Bateman module) for its subsequent transport through the basolateral membrane. However, further studies are needed to confirm this hypothesis.

In the kidney, fine-tuning of serum Mg^{2+} levels occurs via active transcellular Mg^{2+} reabsorption at the DCT. In the DCT, Mg^{2+} is transported from the pre-urine side by the apical TRPM6 channel, through the cytosol, and via an as yet unidentified basolateral extrusion mechanism to the blood [14]. Recent data showed a predominant basolateral CNNM2 expression in the DCT [16,17], and the recently discovered Mg^{2+}-extrusion capability of its closest homologue CNNM4 across intestinal epithelia [20], suggest that CNNM2 could be (part of) this Mg^{2+} extruder or, alternatively, regulate it. The recently discovered Mg^{2+}-extrusion capability of its closest homologue CNNM4 across intestinal epithelia [20] enhances the probability that the MgATP-binding capacity of CNNM2$^{429–584}$ is key in the extrusion of Mg^{2+} ions through the basolateral membrane in the DCT. Taking into account that Mg^{2+} is predominantly complexed to ATP (MgATP), an increase in the intracellular Mg^{2+} concentration may favour binding of MgATP at the S2 cavity of the Bateman module and foster the conformational equilibrium towards the 'flat' state (Figures 5 and 6, and Supplementary Movies S1–S4). In agreement with the co-operative effect between ATP and Mg^{2+} observed by NMR (Figure 2, and Supplementary Figures S2–S4) and crystallography (Figure 4 and Supplementary Figure S7), the electrostatic potential of the protein surface suggests that at high Mg^{2+} concentrations, free Mg^{2+} ions (and probably other metal ions) might complement the effect of MgATP binding by contributing to neutralize the otherwise repulsive forces existing between M3 acidic clusters from complementary monomers in the flat conformer.

Strikingly, we have found that the T568I mutation in CNNM2 that causes familial hypomagnesaemia [16,17] infers a steric hindrance that avoids nucleotide binding at site S2 and disrupts the hydrogen-bond network centred on Thr^{568}, causing a small rearrangement in the orientation of helices H0 and H4 that subsequently favours the flat conformation of the CBS module (Figures 5 and 6). Thus, unexpectedly, the T568I mutation impedes nucleotide binding but mimics the structural effect of binding nucleotides at the CBS module. As shown in the present study, disruption of the intramolecular interactions participated in by Thr^{568}, i.e. by mutation of this residue to isoleucine, impairs the conformational equilibrium of CNNM2$^{429–584}$, which becomes 'locked' in a nucleotide-bound-like state. As a result, the protein dimer remains as a 'flat' disc-like structure that most probably is unable to return to the 'twisted' state, thus becoming non-functional. Consequently, it is reasonable to assume that the function performed by this region of the protein gets hindered by a loss of its natural conformational flexibility. Such failure may be the cause of an impaired transport of Mg^{2+} ions through the basolateral membrane or alternatively alter the regulation of other basolateral transporters which CNNM2 might regulate, leading to hypomagnesaemia. Alternatively, we can speculate that DCT cells with a T568I mutation, even under low intracellular MgATP levels, might falsely sense high MgATP levels. Thus inadvertently high MgATP sensing by CNNM2 in the DCT could be a cause of hypomagnesaemia. Most hereditary primary hypomagnesaemia mechanisms known to date are caused by impaired transcellular Mg^{2+} reabsorption at the renal distal tubule [53], mostly by affecting the apical entry pathway TRPM6 [53–56]. Such an effect on TRPM6 via indirect signalling to the apical side could be the case for the false high MgATP sensing state of the T568I mutation. In such a situation, CNNM2 does not necessarily need to transport Mg^{2+} itself. In light of this it is of particular interest that bacterial CorC, the bacterial orthologue of CNNMs in *Salmonella*, is involved in Mg^{2+} efflux [24], but until now, has never been shown to transport Mg^{2+} itself.

In support of the data of the present study, a report by Hirata et al. [57] published during the revision of the paper, shows that gradual and dose-dependent SPR (surface plasmon resonance) responses using Mg^{2+} itself as an analyte, indicate a direct, although weak, interaction between Mg^{2+} and a truncated protein (CNNM2$^{469–578}$) containing the CBS pair of CNNM2 but lacking the N-terminal helix H0 (see Figure 3). Also, in agreement with the weak interaction that we have detected by NMR, no significant SPR responses are observed at increasing concentrations of ATP in the absence of Mg^{2+}. More interestingly, the authors report

the Mg^{2+}-dependency of ATP binding to the CBS domains of CNNM2, as we have found by means of other techniques. Surprisingly, and in contrast with our NMR and crystallographic data, Hirata et al. [57] claim no AMP-binding capacity for $CNNM2^{469–578}$. This observation contrasts with the role of Mg^{2+} in neutralizing the negative charge of the polyphosphate chain of ATP to favour its binding to site S2, which would otherwise be disfavoured by the presence of the acid cluster formed by residues Glu^{570}, Asp^{571} and Glu^{574}. In this regard, the crystal structure of the AMP–$CNNM2^{429–584}$ complex provides the strongest evidence for specific AMP binding to the Bateman module of CNNM2.

The data of the present study do not assign a definite biological function for CNNM2, but provide the first structural data for members of the cyclin M family and should help to understand the molecular mechanisms by which these proteins mediate the homoeostasis of Mg^{2+} and/or other metal ions as well as the role played by mutations in the development of human disease. It also provides a framework for rational design of drugs that specifically modulate the activity of these proteins. Noteworthily, the conformational change of $CNNM2^{429–584}$ described in the present paper may also help us to understand how MgATP binding to the Bateman module of CNNM3 affects its interaction with protein PRL-2 [58], an important issue to unravel the molecular mechanism by which Mg^{2+} transport may promote tumour progression [58].

AUTHOR CONTRIBUTION

Maria Corral-Rodríguez, Iker Oyenarte, June Ereño-Orbea, Guillermo Abascal-Palacios, Marchel Stuiver and Luis Martínez-Cruz designed and cloned the constructs, purified the proteins and solved the crystal structures. José Antonio Encinar, Vojtech Spiwok, Hiroyuki Terashima and Alessio Accardi performed biophysical studies. Maria Corral-Rodriguez, Alain Ibáñez De Opakua, Francisco Blanco and Tammo Diercks performed NMR analysis. Dominik Müller and Luis Martinez-Cruz designed and supervised research and wrote the paper. All authors contributed to revision of the paper.

ACKNOWLEDGEMENTS

We thank the staff of ESRF (European Synchrotron Radiation Facility, Grenoble, France) beamlines ID14-1 and ID23-1 and Diamond (Didcot, U.K.) beamline I04 for support during synchrotron data collection and also Dr Adriana Rojas for excellent maintenance of the in-house X-ray platform.

FUNDING

This work was supported by the Departamento de Educación, Universidades e Investigación del Gobierno Vasco [grant number PI2010-17], the Departamento de Industria, Innovación, Comercio y Turismo del Gobierno Vasco [grant numbers ETORTEK IE05-147, IE07-202], Diputación Foral de Bizkaia [grant numbers 7/13/08/2006/11, 7/13/08/2005/14], Spanish Ministerio de Ciencia e Innovación (MICINN) [grant number BFU2010-17857] and the MICINN CONSOLIDER-INGENIO 2010 Program [grant number CSD2008-00005] to L.A.M.C. M.S. and D.M. were supported through a grant from the European Community, Framework Programme 7 [grant number EUNEFRON 2011590].

REFERENCES

1 Swaminathan, R. (2003) Magnesium metabolism and its disorders. Clin. Biochem. Rev. **24**, 47–66 PubMed
2 Jahnen-Dechent, W. and Ketteler, M. (2012) Magnesium basics. Clin. Kidney J. **5** (Suppl. 1), i3–i14 CrossRef
3 Quamme, G. A. (2010) Molecular identification of ancient and modern mammalian magnesium transporters. Am. J. Physiol. Cell Physiol. **298**, C407–C429 CrossRef PubMed
4 Günther, T. (1993) Mechanisms and regulation of Mg^{2+} efflux and Mg^{2+} influx. J. Miner. Electrolyte Metab. **19**, 259–265
5 Cefaratti, C., Romani, A. and Scarpa, A. (2000) Differential localization and operation of distinct Mg^{2+} transporters in apical and basolateral sides of rat liver plasma membrane. J. Biol. Chem. **275**, 3772–3780 CrossRef PubMed
6 Romani, A. M. and Scarpa, A. (2000) Regulation of cellular magnesium. Front. Biosci. **5**, D720–D374 CrossRef PubMed
7 Tashiro, M., Konishi, M., Iwamoto, T., Shigekawa, M. and Kurihara, S. (2000) Transport of magnesium by two isoforms of the Na^+-Ca^{2+} exchanger expressed in CCL39 fibroblasts. Pflugers Arch. **440**, 819–827 CrossRef PubMed
8 Watanabe, M., Konishi, M., Ohkido, I. and Matsufuji, S. (2005) Enhanced sodium-dependent extrusion of magnesium in mutant cells established from a mouse renal tubular cell line. Am. J. Physiol. Renal Physiol. **289**, F742–F748 CrossRef PubMed
9 Schweigel, M., Kolisek, M., Nikolic, Z. and Kuzinski, J. (2008) Expression and functional activity of the Na/Mg exchanger, TRPM7 and MagT1 are changed to regulate Mg homeostasis and transport in rumen epithelial cells. Magnes. Res. **21**, 118–123 PubMed
10 Eshaghi, S., Niegowski, D., Kohl, A., Martinez Molina, D., Lesley, S. A. and Nordlund, P. (2006) Crystal structure of a divalent metal ion transporter CorA at 2.9 angstrom resolution. Science **313**, 354–357 CrossRef PubMed
11 Sponder, G., Svidova, S., Schweigel, M., Vormann, J. and Kolisek, M. (2010) Splice-variant 1 of the ancient domain protein 2 (ACDP2) complements the magnesium-deficient growth phenotype of *Salmonella enterica* sv. typhimurium strain MM281. Magnes. Res. **23**, 105–114 PubMed
12 Li, F. Y., Chaigne-Delalande, B., Kanellopoulou, C., Davis, J. C., Matthews, H. F., Douek, D. C., Cohen, J. I., Uzel, G., Su, H. C. and Lenardo, M. J. (2011) Second messenger role for Mg^{2+} revealed by human T-cell immunodeficiency. Nature **475**, 471–476 CrossRef PubMed
13 Rude, R. K. and Gruber, H. E. (2004) Magnesium deficiency and osteoporosis: animal and human observations. J. Nutr. Biochem. **15**, 710–716 CrossRef PubMed
14 Ferrè, S., Hoenderop, J. G. and Bindels, R. J. (2011) Insight into renal Mg^{2+} transporters. Curr. Opin. Nephrol. Hypertens. **20**, 169–176 CrossRef PubMed
15 McKusick, V. A. (1998) Mendelian Inheritance in Man. A Catalog of Human Genes and Genetic Disorders, 12th edn, Johns Hopkins University Press, Baltimore
16 Stuiver, M., Lainez, S., Will, C., Terryn, S., Günzel, D., Debaix, H., Sommer, K., Kopplin, K., Thumfart, J., Kampik, N. B. et al. (2011) CNNM2, encoding a basolateral protein required for renal Mg^{2+} handling, is mutated in dominant hypomagnesemia. Am. J. Hum. Genet. **88**, 333–343 CrossRef PubMed
17 De Baaij, J. H., Stuiver, M., Meij, I. C., Lainez, S., Kopplin, K., Venselaar, H., Müller, D., Bindels, R. J. and Hoenderop, J. G. (2012) Membrane topology and intracellular processing of cyclin M2 (CNNM2). J. Biol. Chem. **287**, 13644–13655 CrossRef PubMed
18 Polok, B., Escher, P., Ambresin, A., Chouery, E, Bolay, S., Meunier, I., Nan, F., Hamel, C., Munier, F. L., Thilo, B. et al. (2009) Mutations in CNNM4 cause recessive cone-rod dystrophy with amelogenesis imperfecta. Am. J. Hum. Genet. **84**, 259–265 CrossRef PubMed
19 Parry, D. A., Mighell, A. J., El-Sayed, W., Shore, R. C., Jalili, I. K., Dollfus, H., Bloch-Zupan, A., Carlos, R., Carr, I. M., Downey, L. M. et al. (2009) Mutations in CNNM4 cause Jalili syndrome, consisting of autosomal-recessive cone-rod dystrophy and amelogenesis imperfecta. Am. J. Hum. Genet. **84**, 266–273 CrossRef PubMed
20 Yamazaki, D., Funato, Y., Miura, J., Sato, S., Toyosawa, S., Furutani, K., Kurachi, Y., Omori, Y., Furukawa, T., Tsuda, T. et al. (2013) Basolateral Mg^{2+} extrusion via CNNM4 mediates transcellular Mg^{2+} transport across epithelia: a mouse model. PLoS Genet. **9**, e1003983 CrossRef PubMed
21 Goytain, A. and Quamme, G. A. (2005) Functional characterization of ACDP2 (ancient conserved domain protein), a divalent metal transporter. Physiol. Genomics **22**, 382–389 CrossRef PubMed
22 Wang, C. Y., Shi, J. D., Yang, P., Kumar, P. G., Li, Q. Z., Run, Q. G., Su, Y. C., Scott, H. S., Kao, K. J. and She, J. X. (2003) Molecular cloning and characterization of a novel gene family of four ancient conserved domain proteins (ACDP). Gene **306**, 37–44 CrossRef PubMed
23 Wang, C. Y., Yang, P., Shi, J. D., Purohit, S., Guo, D., An, H., Gu, J. G., Ling, J., Dong, Z. and She, J. X. (2004) Molecular cloning and characterization of the mouse *Acdp* gene family. BMC Genomics **5**, 1–9 CrossRef PubMed
24 Gibson, M. M., Bagga, D. A., Miller, C. G. and Maguire, M. E. (1991) Magnesium transport in *Salmonella typhimurium*: the influence of new mutations conferring Co^{2+} resistance on the CorA Mg^{2+} transport system. Mol. Microbiol. **5**, 2753–2762 CrossRef PubMed
25 Yang, M., Jensen, L. T., Gardner, A. J. and Culotta, V. C. (2005) Manganese toxicity and *Saccharomyces cerevisiae* Mam3p, a member of the ACDP (ancient conserved domain protein) family. Biochem. J. **386**, 479–487 CrossRef PubMed
26 Bateman, A. (1997) The structure of a domain common to archaebacteria and the homocystinuria disease protein. Trends Biochem. Sci. **22**, 12–13 CrossRef PubMed
27 Scott, J. W., Hawley, S. A., Green, K. A., Anis, M., Stewart, G., Scullion, G. A., Norman, D. G. and Hardie, D. G. (2004) CBS domains form energy-sensing modules whose binding of adenosine ligands is disrupted by disease mutations. J. Clin. Invest. **113**, 274–284 CrossRef PubMed
28 Kemp, B. E. (2004) Bateman modules and adenosine derivatives form a binding contract. J. Clin. Invest. **113**, 182–184 CrossRef PubMed
29 Shabb, J. B. and Corbin, J. D. (1992) Cyclic nucleotide-binding domains in proteins having diverse functions. J. Biol. Chem. **267**, 5723–5726 PubMed

30 Hattori, M., Tanaka, Y., Fukai, S., Ishitani, R. and Nureki, O. (2007) Crystal structure of the MgtE Mg^{2+} transporter. Nature **448**, 1072–1075 CrossRef PubMed
31 Hattori, M., Iwase, N., Furuya, N., Tanaka, Y., Tsukazaki, T., Ishitani, R., Maguire, ME., Ito, K., Maturana, A. and Nureki, O. (2009) Mg^{2+}-dependent gating of bacterial MgtE channel underlies Mg^{2+} homeostasis. EMBO J. **28**, 3602–3612 CrossRef PubMed
32 Ishitani, R., Sugita, Y., Dohmae, N., Furuya, N., Hattori, M. and Nureki, O. (2008) Mg^{2+}-sensing mechanism of Mg^{2+} transporter MgtE probed by molecular dynamics study. Proc. Natl. Acad. Sci. U.S.A. **105**, 15393–15398 CrossRef PubMed
33 Guo, D., Ling, J., Wang, M. H., She, J. X., Gu, J. and Wang, C. Y. (2005) Physical interaction and functional coupling between ACDP4 and the intracellular ion chaperone COX11, an implication of the role of ACDP4 in essential metal ion transport and homeostasis. Mol. Pain **1**, 1–11 CrossRef PubMed
34 Gómez-García, I., Oyenarte, I. and Martínez-Cruz, L. A. (2011) Purification, crystallization and preliminary crystallographic analysis of the CBS pair of the human metal transporter CNNM4. Acta Crystallogr. F Struct. Biol. Commun. **67**, 349–353 CrossRef
35 Gómez-García, I., Stuiver, M., Ereño, J., Oyenarte, I., Corral-Rodríguez, M. A., Müller, D. and Martínez-Cruz, L. A. (2012) Purification, crystallization and preliminary crystallographic analysis of the CBS-domain pair of cyclin M2 (CNNM2). Acta Crystallogr. F Struct. Biol. Commun. **68**, 1198–1203 CrossRef
36 Marley, J., Lu, M. and Bracken, C. (2001) A method for efficient isotopic labeling of recombinant proteins. J. Biomol. NMR **20**, 71–75 CrossRef PubMed
37 Otwinowski, Z. and Minor, W. (1997) Processing of X-ray diffraction data collected in oscillation mode. Methods Enzymol. **276**, 307–326 CrossRef
38 McCoy, A. J., Grosse-Kunstleve, R. W., Adams, P. D., Winn, M. D., Storoni, L. C. and Read, R. J. (2007) Phaser crystallographic software. J. Appl. Crystallogr. **40**, 658–674 CrossRef PubMed
39 Lucas, M., Encinar, J. A., Arribas, E. A., Oyenarte, I., García, I. G., Kortazar, D., Fernández, J. A., Mato, J. M., Martínez-Chantar, M. L. and Martínez-Cruz, L. A. (2010) Binding of *S*-methyl-5′-thioadenosine and *S*-adenosyl-L-methionine to protein MJ0100 triggers an open-to-closed conformational change in its CBS motif pair. J. Mol. Biol. **396**, 800–820 CrossRef PubMed
40 Zwart, P. H., Afonine, P. V., Grosse-Kunstleve, R. W., Hung, L. W., Ioerger, T. R., McCoy, A. J., McKee, E., Moriarty, N. W., Read, R. J., Sacchettini, J. C. et al. (2008) Automated structure solution with the PHENIX suite. Methods Mol. Biol. **426**, 419–435 CrossRef PubMed
41 Vagin, A. A., Steiner, R. S., Lebedev, A. A., Potterton, L., McNicholas, S., Long, F. and Murshudov, G. N. (2004) REFMAC5 dictionary: organisation of prior chemical knowledge and guidelines for its use. Acta Crystallogr. D Biol. Crystallogr. **60**, 2284–2295 CrossRef
42 Emsley, P. and Cowtan, K. (2004) Coot: model-building tools for molecular graphics. Acta Crystallogr. D Biol. Crystallogr. **60**, 2126–2132 CrossRef PubMed
43 Chen, V. B., Arendall, 3rd, W. B., Headd, J. J., Keedy, D. A., Immormino, R. M., Kapral, G. J., Murray, L. W., Richardson, J. S. and Richardson, D. C. (2010) MolProbity: all-atom structure validation for macromolecular crystallography. Acta Crystallogr. D Biol. Crystallogr. **66**, 12–21 CrossRef PubMed
44 Reference deleted
45 Ignoul, S. and Eggermont, J. (2005) CBS domains: structure, function, and pathology in human proteins. Am. J. Physiol. Cell Physiol. **289**, C1369–C1378 CrossRef PubMed
46 Baykov, A. A., Tuominen, H. K. and Lahti, R. (2011) The CBS domain: a protein module with an emerging prominent role in regulation. ACS Chem. Biol. **6**, 1156–1163 CrossRef PubMed
47 Ereño-Orbea, J., Oyenarte, I. and Martínez-Cruz, L. A. (2013) CBS domains: ligand binding sites and conformational variability. Arch. Biochem. Biophys. **540**, 70–81 CrossRef PubMed
48 Gómez-García, I., Oyenarte, I. and Martínez-Cruz, L. A. (2010) The crystal structure of protein MJ1225 from *Methanocaldococcus jannaschii* shows strong conservation of key structural features seen in the eukaryal γ-AMPK. J. Mol. Biol. **399**, 53–70 CrossRef PubMed
49 Beis, I. and Newsholme, E. A. (1975) The contents of adenine nucleotides, phosphagens and some glycolytic intermediates in resting muscles from vertebrates and invertebrates. Biochem. J. **152**, 23–32 PubMed
50 Sigel, H. (1987) Isomeric equilibria in complexes of adenosine 5′-triphosphate with divalent metal ions. Solution structures of $M(ATP)^{2-}$ complexes. Eur. J. Biochem. **165**, 65–72 CrossRef PubMed
51 Hung, L. W., Wang, I. X., Nikaido, K., Liu, P. Q., Ames, G. F. and Kim, S. H. (1998) Crystal structure of the ATP-binding subunit of ABC transporter. Nature **396**, 703–707 CrossRef PubMed
52 Wu, S. L., Li, C. C., Chen, J. C., Chen, Y. J., Lin, C. T., Ho, T. Y. and Hsiang, C. Y. (2009) Mutagenesis identifies the critical amino acid residues of human endonuclease G involved in catalysis, magnesium coordination, and substrate specificity. J. Biomed. Sci. **16**, 6 CrossRef PubMed
53 San-Cristobal, P., Dimke, H., Hoenderop, J. G. and Bindels, R. J. (2010) Novel molecular pathways in renal Mg^{2+} transport: a guided tour along the nephron. Curr. Opin. Nephrol. Hypertens. **19**, 456–462 CrossRef PubMed
54 Voets, T., Nilius, B., Hoefs, S., van der Kemp, A. W, Droogmans, G, Bindels, R. J. and Hoenderop, J. G. (2004) TRPM6 forms the Mg^{2+} influx channel involved in intestinal and renal Mg^{2+} absorption. J. Biol. Chem. **279**, 19–25 CrossRef PubMed
55 Li, M., Jiang, J. and Yue, L. (2006) Functional characterization of homo- and heteromeric channel kinases TRPM6 and TRPM7. J. Gen. Physiol. **127**, 525–537 CrossRef PubMed
56 Li, M., Du, J., Jiang, J., Ratzan, W., Su, L. T., Runnels, L. W. and Yue, L. (2007) Molecular determinants of Mg^{2+} and Ca^{2+} permeability and pH sensitivity in TRPM6 and TRPM7. J. Biol. Chem. **282**, 25817–25830 CrossRef PubMed
57 Hirata, Y., Funato, Y., Takano, Y. and Miki, H. (2014) Mg^{2+}-dependent interactions of ATP with the cystathionine-β-synthase (CBS) comains of a magnesium transporter. J. Biol. Chem. **289**, 14731–14739 CrossRef PubMed
58 Hardy, S., Uetani, N., Wong, N., Kostantin, E., Labbé, D. P., Bégin, L. R., Mes-Masson, A., Miranda-Saavedra, D. and Tremblay, M. L. (2014) The protein tyrosine phosphatase PRL-2 interacts with the magnesium transporter CNNM3 to promote oncogenesis. Oncogene, doi: 10.1038/onc.2014.33

Received 28 March 2014/4 August 2014; accepted 3 September 2014
Published as BJ Immediate Publication 3 September 2014, doi:10.1042/BJ20140409

SUPPLEMENTAL DATA

Figure S1. Effect of Mg^{2+} on $CNNM2_{429-584}$. The ^{15}N HSQC spectrum of $CNNM2_{429-584}$ in the absence of Mg^{2+} (*black*) is overlapped with that obtained after addition of 2.5 mM $MgCl_2$ (*green*). Increasing concentrations of $MgCl_2$ from 2.5 → to 10 mM do not produce further significant spectral changes. The protein concentration is 200 μM. Numbers 1 to 5 refer to each of the five groups of signals discussed in Figure 2.

Figure S2. Effect of ATP on $CNNM2_{429-584}$. ^{15}N HSQC spectrum of $CNNM2_{429-584}$ at increasing concentrations of ATP. The spectrum in the absence of ATP (*black*) is overlapped with those obtained after addition of 500 μM ATP (*red*), and 10 mM ATP (*magenta*). Spectral changes caused by addition of 500 μM ATP (*black arrows*) indicate specific protein-ligand interactions. No further changes are observed between 500 μM → 2.5 mM ATP. Noteworthy, increasing the ATP concentration to 10 mM induces some additional peak shifts (*pink arrows*). The protein concentration is 200 μM. Numbers 1 to 5 refer to each of the five groups of signals discussed in Figure 2.

Figure S3. Effect of co-addition of Mg^{2+} and ATP to $CNNM2_{429-584}$. The ^{15}N HSQC spectrum of $CNNM2_{429-584}$ obtained in the absence of Mg^{2+} (*black*) is overlapped with the spectra obtained after

addition of 2.5 mM ADPNP + 0.5 mM $MgCl_2$ (*green*); 2.5 mM ADPNP + 1 mM $MgCl_2$ (*orange*); and 2.5 mM ADPNP + 2.5 mM $MgCl_2$ (*red*). The protein concentration is 200 μM in all cases. Numbers 1 to 5 refer to each of the five groups of signals discussed in Figure 2.

Figure S4. Effect of ATP at high Mg^{2+} concentrations. The ^{15}N HSQC spectrum of $CNNM2_{429-584}$ obtained in the absence of Mg^{2+} (*black*) is overlapped with the spectra obtained at 10 mM $MgCl_2$ + 2.5 mM ADPNP (*red*) or 2.5 mM ADPNP + 10 mM $MgCl_2$ (*blue*). Numbers 1 to 5 refer to each of the five groups of signals discussed in Figure 2.

Figure S5. Effect of AMP on $CNNM2_{429-584}$. The ^{15}N HSQC spectrum of $CNNM2_{429-584}$ obtained in the absence of Mg^{2+} (*black*) is overlapped with the spectrum obtained after addition of 5 mM AMP (*blue*). The protein concentration is 200 μM. Numbers 1 to 5 refer to each of the five groups of signals discussed in Figure 2.

Figure S6. Residues forming the cavity S1 in $CNNM2_{429-584}$.

Figure S7. Nucleotide binding site S2 in $CNNM2_{429-584}$. **(A)** MgATP-binding site as observed in the $P4_32_12$ crystals (PDB code 4P1O; Table 1). The Fo-Fc map contoured at 3.0 σ shows residual density for MgATP (omitted in the refined model). **(B)** After including ATP in the refinement protocol, the Fo-Fc map contoured at 3.0 σ shows the residual density found for Mg^{2+}. The absence of $MgCl_2$ in the crystallization drop, results in the loss of this electron density.

Figure S8. ATP binding site in $CNNM2_{429-584}$ and ABC transporters. Structural comparison of (A) the ATP binding site S2 of $CNNM2_{429-584}$ and (B) the ATP binding site of the histidine permease from *Salmonella typhimurium* (PDB code 1B0U) [51]. Loops Walker A (in *red*) and Walker B (in

blue) provide the key residues involved in ATP hydrolysis in the bacterial ABC transporter [51]. Of note, clusters of negatively charged (E570-D571-E574), and positively charged (i.e H544-R480 and H211-K45) residues, occupy equivalent positions in both ATP sites. Similarly, serine or threonine residues (T479-T568; S41-T47), together with a conserved lysine (K45) or arginine (R480) contribute to stabilize the polyphosphate chain of ATP in a defined orientation. The main differences between the two proteins arise in the upper part of the cavity, which host the adenine and ribose rings. In $CNNM2_{429-584}$, the hydroxyl groups of ribose interact with a conserved carboxylate residue of the acidic cluster (D571), and with a threonine (T451) donated by the loop connecting helices HA_1 and HA_2 (see Fig. 3), whereas a histidine residue (H19) located in the opposite side of the site helps orienting the ribose in the histidine permease (Fig. S8).

Movie S1. The movie reproduces the conformational change suffered by helices H0 (on the left) and H4 (in the centre) upon binding nucleotides in the $CNNM2_{429-584}$ monomer (see also Figs. 3, 4). *Apo*-$CNNM2_{429-584}$ is represented in *grey*. The nucleotide-bound CNNM2 is in *yellow*. These structural changes suffered by the protein monomer are further transmitted to the dimer interface making it to progress from a "twisted" to a "flat" conformation (see Fig. 5; movies S2 to S4). Along the process, several salt link interactions are disrupted (i. e E570-R480 in the centre), while new ones are formed (i.e K578-E575-K444-E440 on the left).

Movies S2, S3 and S4. The movies reproduce three different views of the conformational change triggered by AMP/ADP/ATP/MgATP-binding in the CBS module of $CNNM2_{429-584}$. The CBS module evolves from a "twisted" to a "flat" conformation upon binding of nucleotides (not represented) at site S2, containing residue D571. In movie S1, helices H0 (placed in front) from both monomers act as a hinge while the conformational change occurs. Movie S2 shows a top view. In this case, helices H0 are place in the upper part of the figure. The CBS 1 motifs from each monomer

are separated and become closer upon binding of the nucleotide (not represented). Movie S3 shows a side view of the CBS module, turned 180 degrees with respect to that shown in Movie S1.

Figure S1.

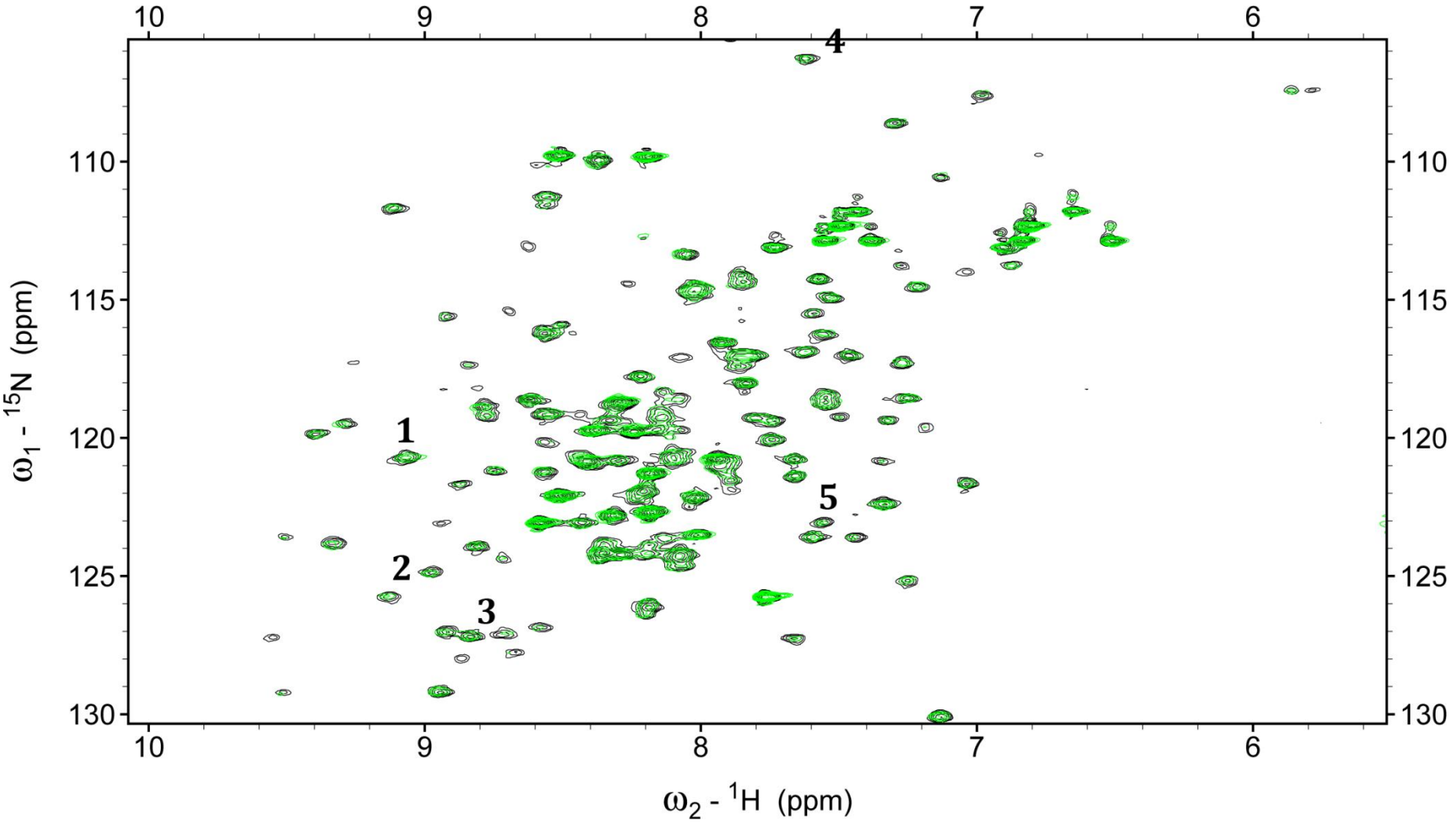

Figure S2.

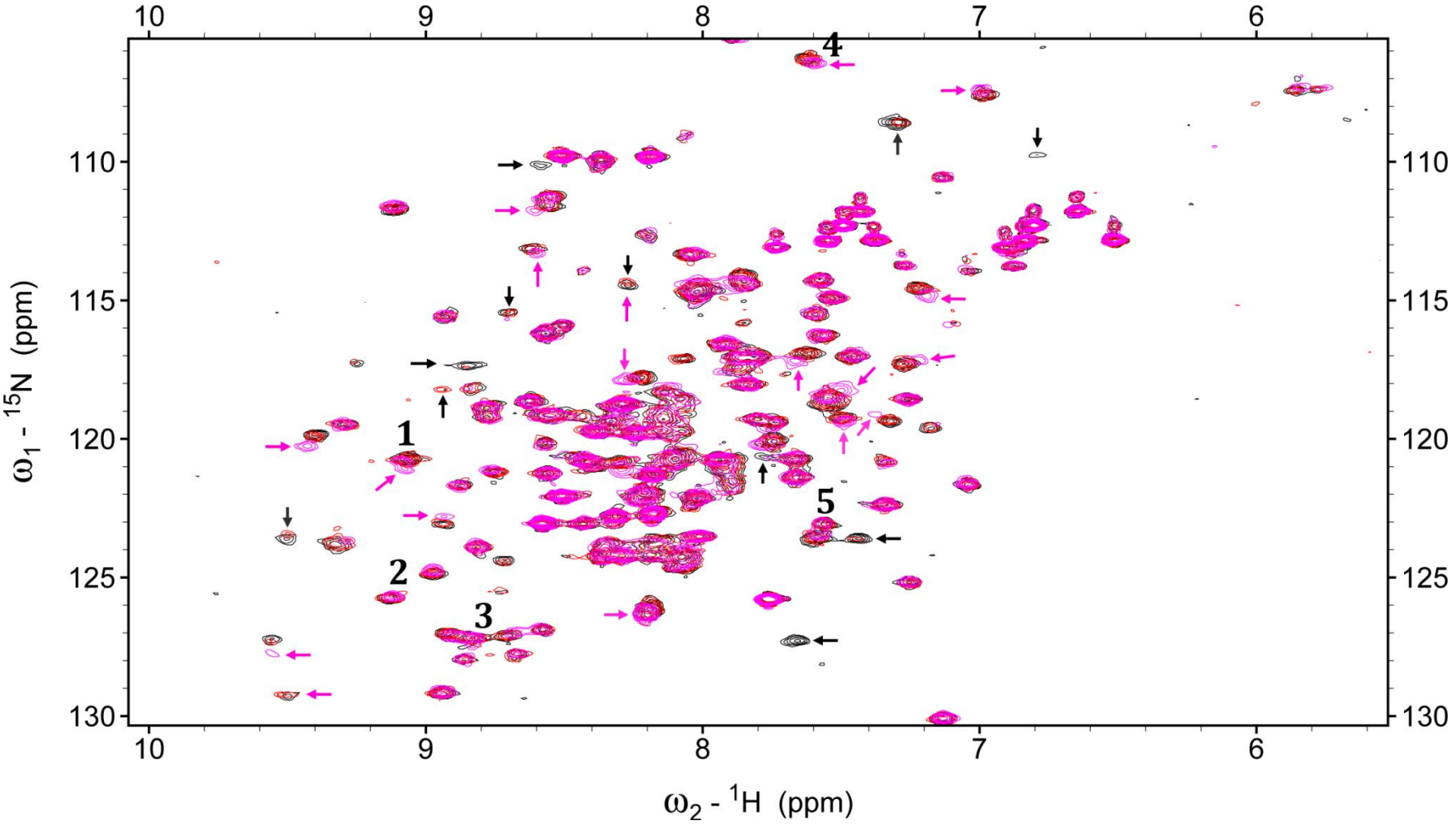

Figure S3.

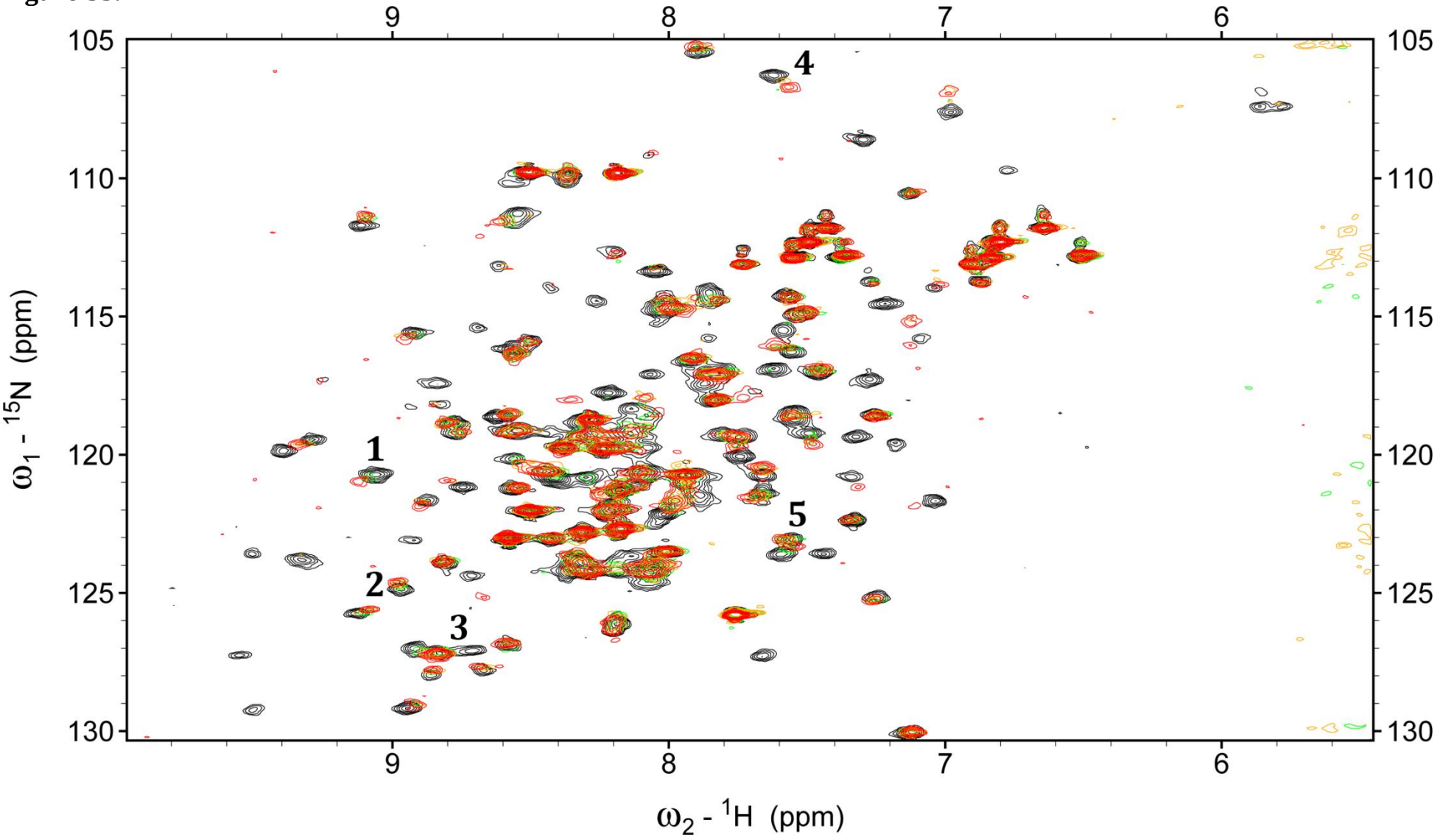
9
8
7
6
105
110
115
120
125
130
ω_1 - ^{15}N (ppm)
ω_2 - ^{1}H (ppm)
1
2
3
4
5

Figure S4.

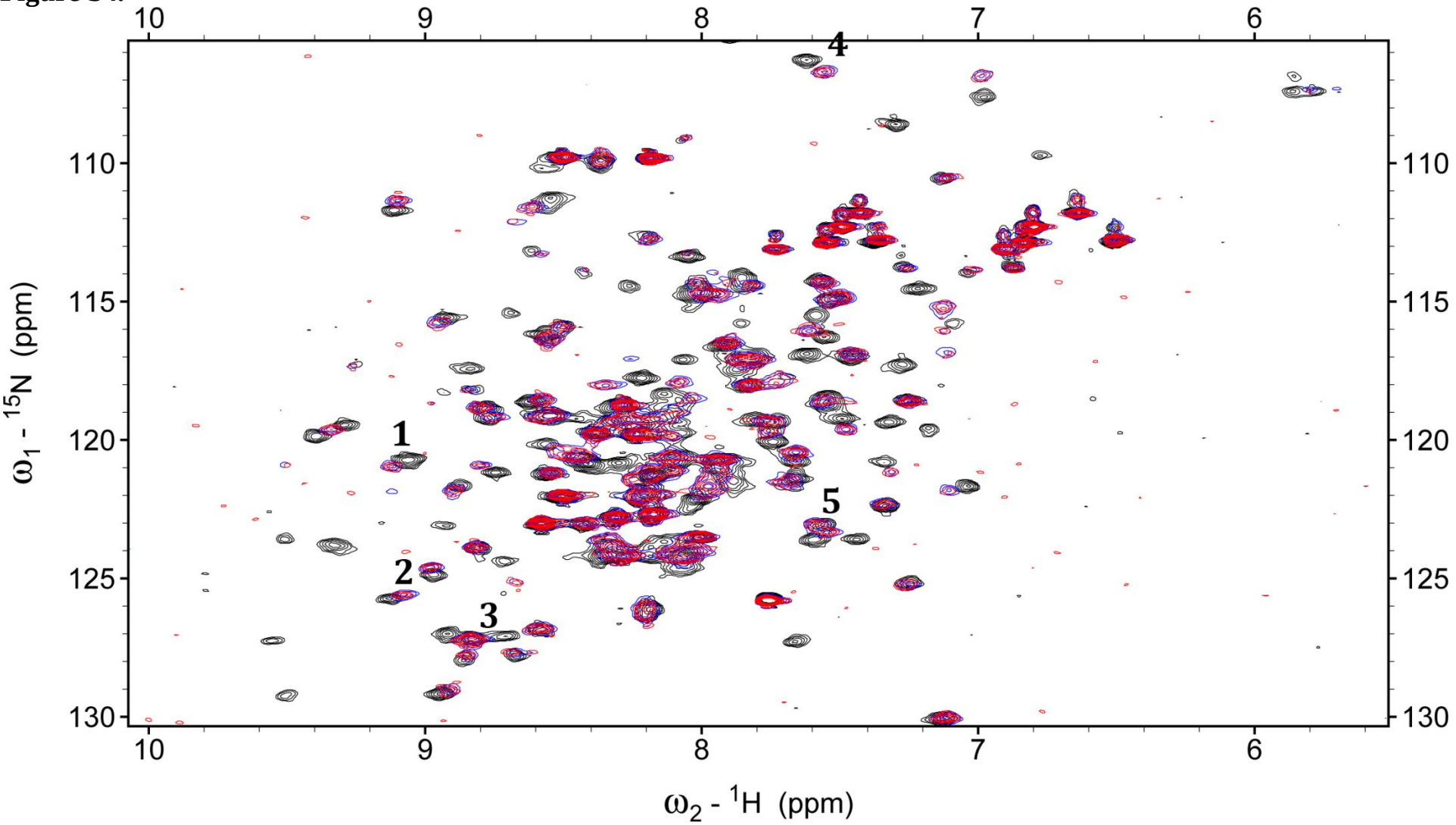

Figure S5.

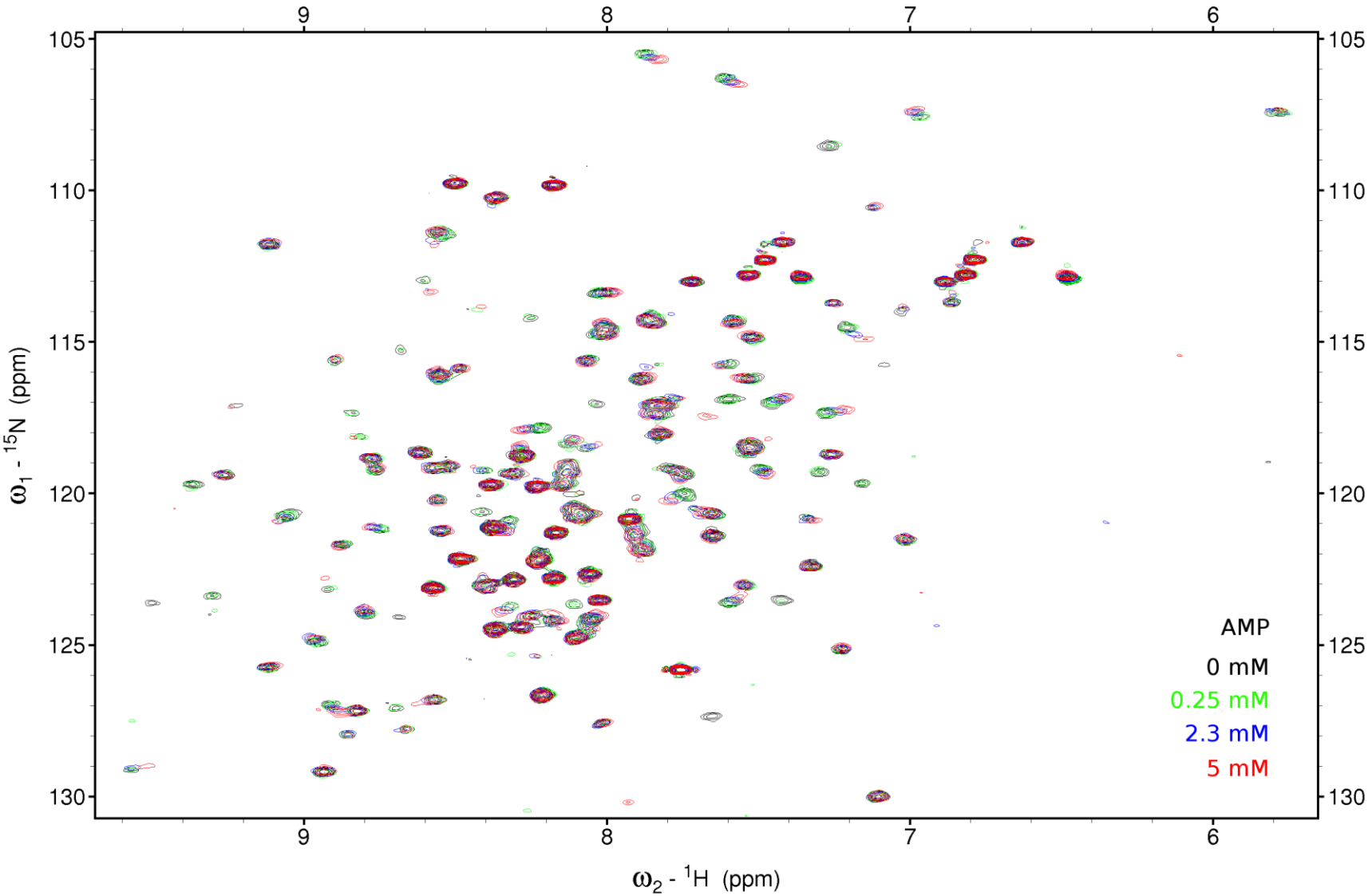
9
8
7
6
105
110
115
120
125
130
ω_1 - ^{15}N (ppm)
ω_2 - ^{1}H (ppm)
AMP
0 mM
0.25 mM
2.3 mM
5 mM

Figure S6.

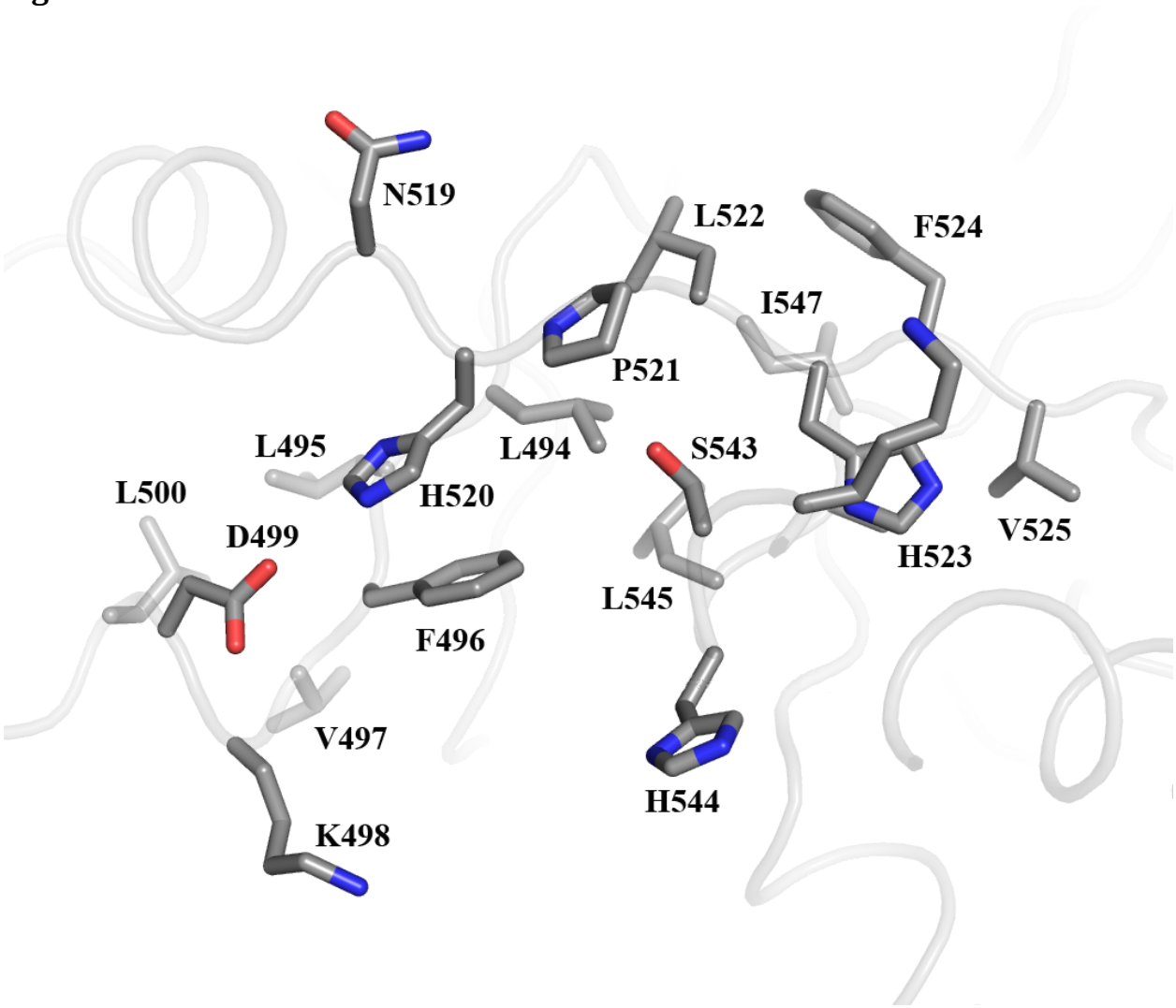
N519
L522
F524
I547
P521
L495
L494
S543
L500
H520
D499
V525
H523
L545
F496
V497
H544
K498

Figure S7.

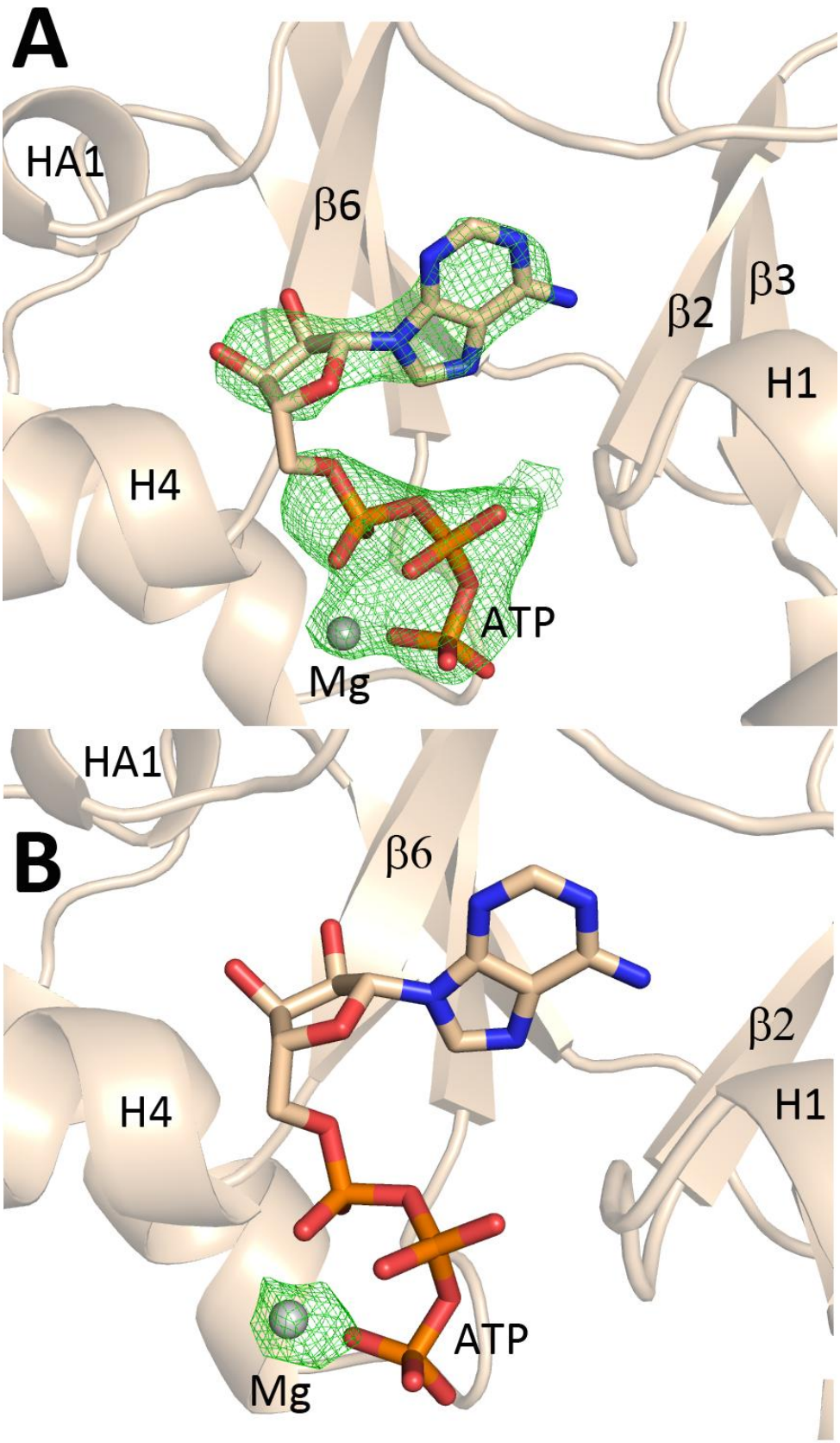

Figure S8.

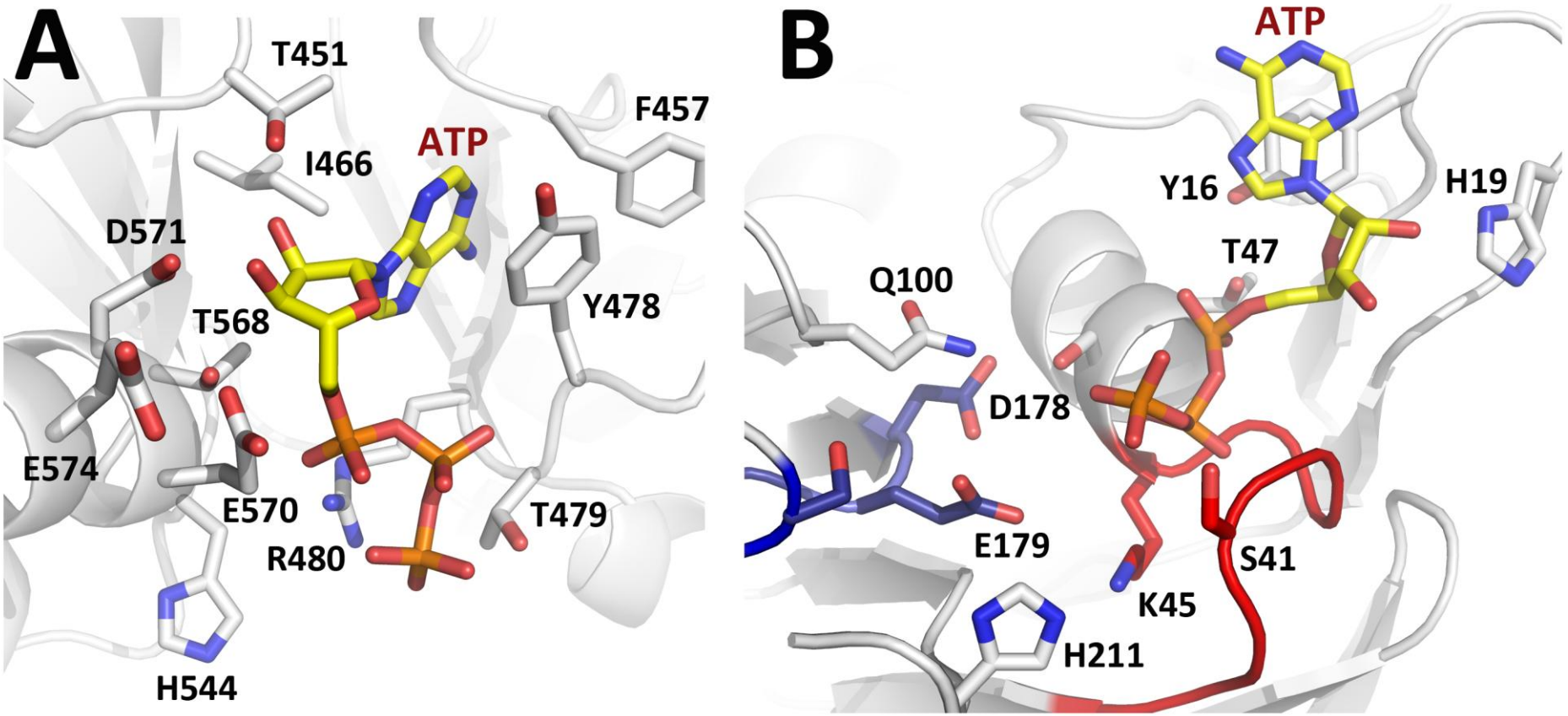
A
T451
F457
ATP
I466
D571
Y478
T568
E574
E570
T479
R480
H544
B
ATP
Y16
H19
T47
Q100
D178
E179
S41
K45
H211